T-4798

Alloy Diffuse Scattering Studied by Small-Angle X-ray Scattering

ARTHUR LAKES LIBRARY
COLORADO SCHOOL OF MINES
GOLDEN, CO 80401

By
Min, Dong-Hoon

ProQuest Number: 10794154

All rights reserved

INFORMATION TO ALL USERS
The quality of this reproduction is dependent upon the quality of the copy submitted.

In the unlikely event that the author did not send a complete manuscript
and there are missing pages, these will be noted. Also, if material had to be removed,
a note will indicate the deletion.

ProQuest 10794154

Published by ProQuest LLC (2018). Copyright of the Dissertation is held by the Author.

All rights reserved.
This work is protected against unauthorized copying under Title 17, United States Code
Microform Edition © ProQuest LLC.

ProQuest LLC.
789 East Eisenhower Parkway
P.O. Box 1346
Ann Arbor, MI 48106 – 1346

T-4798

A thesis submitted to the Faculty and the Board of Trustees of the Colorado school of Mines in partial fulfillment of the requirements for the degree of Master of Science (Physics).

Golden, Colorado

Date: 6/15/95

Signed: Min Dong Hoon

Min, Dong-Hoon

Golden, Colorado

Date: 6/15/95

Approved: Don L. Williamson

Dr. Don L. Williamson

Thesis Advisor

Golden, Colorado

Date: 6/15/95

John U. Trefny

Dr. John U. Trefny

Head of Physics Dept.

Abstract

Germanium clustering in amorphous $Si_{1-x}Ge_x$ alloys, an important material for thin film solar cells, may play a role in the known degradation of the opto-electronic properties with increasing x. Small-angle x-ray scattering (SAXS) might be a useful technique to investigate the possible clustering behavior of Ge. To establish the viability of SAXS for this problem, the crystalline $Al_{1-x}Ga_x$ alloy system was selected as a model for experimental and theoretical study. Ga has high solubility (about 9 at.%) at room temperature according to the published phase diagram and the elements Al and Ga are adjacent to Si and Ge in the periodic table. The primary objective was to establish the ability of SAXS measurements to determine the diffuse scattering intensity due to the Laue monotonic scattering contribution which is simply related to alloy randomness. Several other diffuse scattering mechanisms may contribute so a combined theoretical and experimental approach was used to extract the Laue term. Also the role of the SAXS beam geometry in the conversion to absolute electron intensity units was considered. A series of 5 alloys with x=0, 0.025, 0.050, 0.070 and 0.100 was prepared and carefully examined by SAXS and x-ray diffraction (XRD). Different heat

treatments were used to seek the most random Ga distributions. Good agreement between theory and experiment was found for $x \leq 0.05$, consistent with completely random mixtures of Al and Ga, while clear evidence of Ga precipitation was found for higher x. The effect of x on the lattice parameter of $Al_{1-x}Ga_x$ alloys has been measured to high precision on the basis of the combined SAXS and XRD analyses. The results demonstrate that SAXS can be used to investigate atomic-scale alloy randomness in the amorphous $Si_{1-x}Ge_x$ alloys and they establish the accuracy expected.

Table of Contents

page

Abstract..iii

List of Figures...viii

List of Tables..x

Acknowledgments...xii

Chapter 1. Introduction 1

1.1 Small-Angle X-ray scattering research program at Colorado School of Mines. 1

1.2 Purpose. 2

1.3 Choice of $Al_{1-x}Ga_x$ alloys. 4

1.4 Approach. 4

Chapter 2. Theoretical Background 6

2.1 Scattering mechanisms. 6

2.1.1 Laue monotonic scattering. 8

2.1.2 Incoherent Compton scattering. 9

2.1.3 Thermal diffuse scattering (TDS). 11

2.1.4 Double Bragg scattering (DBS). 12

2.1.5 Dislocation scattering. 14

2.2 Slit collimation. 14

2.2.1 Beam profile. 15

2.2.2 Two-Phase model. 16

2.2.3 Test of infinite slit approximation. 17

Chapter 3. Aluminum Gallium System......................20

3.1 Aluminum-Gallium binary phase diagram. 20

3.2 Diffusion of Ga in Al. 22

3.3 Lattice diffusion of Ga in Al. 24

Chapter 4. Experiment..................................26

4.1 Description of Small-Angle scattering equipment. 26

4.2 Preparation of $Al_{1-x}Ga_x$ alloys. 28

4.2.1 Preparation of the Al and Ga. 28

4.2.2 Melting and step-cooling. 31

4.2.3 Sample rolling and heat treatment. 34

4.3 SAXS data reduction procedures. 35

4.3.1 Intensity normalization. 35

4.3.2 Conversion of normalized intensity to absolute units. 37

4.4 Measurement of the slit function F(x). 38

4.5 Test of slit smearing of lupolen. 39

4.6 X-ray diffraction (XRD). 39

Chapter 5. Results.......................................41

5.1 Slit smearing. 41

5.1.1 Slit length weighting function. 41

5.1.2 Smearing test using P(t). 44

5.1.3 Infinite slit approximation. 44

5.2 Pure Al scattering mechanisms. 47

5.3 $Al_{1-x}Ga_x$ alloys. 50

5.3.1 X-ray Diffraction (XRD). 50

5.3.2 SAXS results for $Al_{1-x}Ga_x$ alloys. 55

5.3.3 Correction of Lattice parameter data by SAXS results. 63

Chapter 6. Summary and Conclusion 66

References. 70

List of Figures

page

Fig. 3.1--Aluminum gallium phase diagram by Murray 21

Fig. 4.1--Schematic diagram of SAXS system 27

Fig. 4.2--Schematic diagram of Ga inside of Al block ..29

Fig. 4.3--Schematic diagram of graphite boat (a) and furnace (b) 32

Fig. 4.4--Melting and step cooling diagram of AlGa 33

Fig. 5.1--Results of beam profile. (a) F(x) and F'(x') which is convoluted from fitted function F(x). (b) P(t) which is a transform of F'(x'). 43

Fig. 5.2--The results of slit smearing effect of standard polyethylene sample (Lupolen). 45

Fig. 5.3--Ratio Q_{fin}/Q versus radius of particle R. 46

Fig. 5.4--SAXS data from pure Al sample #1a and various theoretical contributions. 48

Fig. 5.5--Pure Al SAXS data after subtraction of I_{td}, I_{DBS}, and I_{ic} 49

Fig. 5.6--X-ray diffraction data from as-rolled $Al_{1-x}Ga_x$ alloys. 51

Fig.5.7--Alloy lattice parameters versus Ga atomic fraction x. 52

Fig. 5.8--(a) SAXS intensity of as-rolled series. (b) SAXS intensity after subtraction of pure Al. 56

Fig. 5.9--(a) SAXS intensity of annealed series. (b) SAXS intensity after subtraction of pure Al. 57

Fig. 5.10--Theoretical and experimental Laue monotonic intensities for $Al_{1-x}Ga_x$ alloys. 60

Fig. 5.11--Lattice parameter versus Ga atomic fraction x after correction of x by SAXS results. ...65

List of Tables

page

Table 3.1--Equilibrium maximum solid solubility of Ga in Al for different temperatures (from the phase diagram of Murray). 22

Table 3.2--Lattice diffusion coefficient of Ga in Al at various temperatures. 25

Table 4.2.1--Mass of Al and Ga of each alloy and the total mass before and after melt. 30

Table 4.2.2--Labels of $Al_{1-x}Ga_x$ alloys. 35

Table 5.1--The change of lattice parameters with x increase just after the cold-work and annealing (400°C ×5 hr). 54

Table 5.2--Volume fraction and Q value for each alloy. 59

Table 5.3--Experimental alloy scattering intensities in electron units. (a) as-rolled samples (b) annealed samples. 59

Table 5.4--Amount of Ga in solid solution (x_s) and as Ga precipitates (x_p) based on (a) difference in experimental and theoretical I_{LM} and (b) experimental integrated SAXS intensities. 61

Table 5.5--The integral invariant ratio Q_0/Q_{45} with increase of x. 63

Acknowledgments

I would like to express my sincere appreciation to Dr. Don L. Williamson of the Colorado School of Mines for his continuous advice and endless patience without which this work could not have been completed. I would also like to thank Dr. T. E. Furtak and Dr. John U. Trefny for their helpful remarks and discussions and for serving on my committee.

I am very grateful to the National Renewable Energy Laboratory (NREL) for the financial support.

A special thanks to my parents and Dr. Sung-Ho, Lee and Young-Heum Zhu for their continuous advice. I would also like to thank my friends Dal-Suk, Nag-Hyung, Chang-Yong, Han-Cheul and Hae-Kyung for their helpful advice.

Finally, I would like to thank to all the faculty and staff of the Physics Department at CSM.

To my parents and grand mother, Byung-jun Kim, brother, Jea-Hoon Min, and sister, Yu-Jeung Min who helped me through my academic career.

Chapter 1

Introduction

1.1 Small-Angle X-ray Scattering Research program at the Colorado School of Mines

Small angle X-ray scattering (SAXS) is one of the well-known experimental tools widely used to study the microstructure of materials based on wave diffraction phenomena. Microstructural features such as microvoids, alloy segregation, or precipitation can change the optical and electrical properties of materials. The SAXS technique can provide structural information for samples in which electron density fluctuations occur on a scale of about 1 nm to 100 nm.

A research program focused on the determination of the microstructure of amorphous(a)-Si-based semiconductors is in progress at the Colorado School of Mines, sponsored by NREL (National Renewable Energy Laboratory). One of the major issues within this program is to study whether SAXS-determined microstructure is responsible for the alloy-induced degradation of the opto-electronic properties of a-Si alloys, especially in a-SiGe:H and a-SiC:H materials.

One of the important applications of a-Si-based thin films is to supplement or replace conventional energy sources by the conversion of sunlight into electrical power

using high efficiency, low cost and pollution free solar cells. There are also many other applications such as thin film transistors, electrophotography devices, memory switches and light-emitting devices.

In the a-Si-based semiconductor family, alloying with C and Ge is useful for raising and lowering the optical bandgap, respectively. However, addition of C and Ge generally lead to degradation of the opto-electronic properties that are important for device applications. Little is known about the atomic-scale structure of these alloys. The alloy diffuse scattering contribution to SAXS intensities offers a potential new method for examining the atomic-scale structure of such materials and was considered carefully in this study. Accurate measurements and interpretation of this contribution to the SAXS could lead to new information relevant to understanding the alloy degradation effects.

1.2. Purpose.

Most materials which are dealt with in our NREL-supported research are $a-Si_{1-x-y}Ge_xH_y$, $a-Si_{1-x-y}C_xH_y$, or $a-Si_{1-y}H_y$, consisting of two or more elements in a wide range of composition. The atomic scale electron density fluctuations cause alloy diffuse scattering that is

composition dependent. In this thesis, an investigation will be made of the SAXS-determined alloy scattering from aluminum-gallium binary alloys as a model system. The major goals are to establish the accuracy with which this contribution may be extracted from SAXS data and to test the agreement with available theory. As the gallium content of the alloy is increased from 0 at% to 10 at%, the changes in alloy scattering intensities will be carefully investigated. The results should establish the potential of using such intensities to improve our understanding of the a-Si-based alloys mentioned above.

Some preliminary work addressing the alloy scattering issue by SAXS was done by Chen using a-SiGe:H and a-SiC:H samples [1]. Chen compared the SAXS-determined alloy scattering intensities and theoretically calculated scattering intensities. However, the conversion to absolute electron units was not checked or calibrated by some independent tests. Also considered in this thesis are additional diffuse scattering mechanisms that may contribute to measured scattering intensities and were not discussed by Chen [1].

1.3 Choice of Aluminum Gallium System ($Al_{1-x}Ga_x$)

The Al-Ga alloy system is chosen as a model system for the following reasons. The solubility of gallium in aluminum is 8.8 at% at room temperature [16]. This high solubility is probably due to the fact that Al and Ga are in the same column of the periodic table and their atomic radii are nearly equal. Thus, random alloys are expected for $x < 0.088$ and the Laue monotonic expression should be valid. Preparation of thin foils should be straightforward with available equipment and materials. Also, the $Al_{1-x}Ga_x$ system is close in atomic number to the amorphous $Si_{1-x}Ge_x$ semiconductor alloys of interest in the related work at CSM. The accurate determination of the diffuse scattering from the random $Al_{1-x}Ga_x$ alloys should lead to a determination of whether the $a-Si_{1-x}Ge_x:H$ alloys being developed for solar cells are random or not. This may be a critical issue with respect to their opto-electronic properties.

1.4 Approach

The approach taken in this thesis research involves the following five steps:

i) Investigation of the slit-length smearing contribution to SAXS measured intensities. This involves careful beam profile study and is relevant to absolute intensity units.

ii) Preparation of a set of $Al_{1-x}Ga_x$ alloys and characterization by standard X-ray diffraction. The X-ray diffraction provides lattice parameters and helps determine whether the alloys contain a second phase (Ga precipitates).

iii) Conversion of the measured intensities to absolute electron units (for ease of comparison to theory).

iv) Comparison between the measured SAXS intensities and the theoretically calculated intensities of the model system, i.e. $Al_{1-x}Ga_x$ alloys.

v) Analysis of alloy randomness from the measured SAXS intensities and the X-ray diffraction data of the $Al_{1-x}Ga_x$ alloys.

Chapter 2

Theoretical Background

2.1 Scattering Mechanisms

When we define an electron density function, $\rho(\vec{r})$, at location $\vec{r}$, and average electron density $\overline{\rho}$ over the volume of concern, the difference between $\rho(\vec{r})$ and $\overline{\rho}$ is called the electron density fluctuation function, $\eta(\vec{r})$, at location $\vec{r}$. $\eta(\vec{r})$ causes the SAXS signals, which vary with scattering angle depending on the scale and magnitude of the fluctuations. The X-ray intensity scattered from a material at angle 2θ relative to the incident beam is written as a function of the momentum transfer, $q = \frac{4\pi\sin\theta}{\lambda}$ (λ is the X-ray wavelength). It is useful to separate the measured scattered intensity, $I_{me}(q)$, into two distinct components in the low angle region ($q \leq 6$ nm^{-1}):

$$I_{me}(q) = I_M(q) + I_D(q), \qquad (2.1)$$

where I_M represents the scattered intensity due to the electron density fluctuations on a microstructural scale from about 1 nm to about $\frac{\pi}{q_{min}}$. The q_{min} is the smallest q

accessible by an experiment. Typically, $\frac{\pi}{q_{min}}$ is about 30 nm in the CSM system.

I_D represents the diffuse intensity from electron density fluctuations on a scale less than 1 nm. Diffuse scattering implies little or no angle dependence, and in the literature is often ignored or just subtracted assuming it is a constant background and no longer considered in the analysis of the usual quantity of interest, $I_M(q)$. Here, I_D is of primary interest and it is subdivided into three distinct contributions:

$$I_D = I_{ic} + I_{td} + I_{LM}, \qquad (2.2)$$

where I_{ic} is the incoherent Compton scattering, I_{td} is the thermal diffuse component, and I_{LM} is the Laue monotonic diffuse contribution. I_{LM} is the focus of this research. The next three sections will develop theoretical expressions for each of the diffuse contributions. The expressions and magnitudes will be given in electron units (eu). There are more scattering mechanisms that need to be considered for polycrystalline samples, double Bragg scattering (DBS) and dislocation scattering, both dependent on q. This scattering may be important in cold-worked (e.g. rolled) metal. The

details of these mechanisms will be developed in sections 2.1.4 and 2.1.5 for pure Al.

2.1.1 Laue Monotonic Scattering

When we consider a sample consisting of more than one element, there is X-ray diffuse scattering known as Laue monotonic scattering. Assume there is a simple lattice whose nodes are occupied by different atoms A and B in the relative atomic fractions C_A and C_B, the atomic form factors being f_A and f_B. If the A and B atoms are randomly distributed, there is no extra peak, but instead a weak continuous background. This is called Laue monotonic scattering. Under the assumption of a perfectly random alloy, the Laue monotonic scattering intensity in electron units can be written as [2]

$$I_{LM}(\text{random})=C_A C_B (f_B-f_A)^2. \tag{2.3}$$

When we consider the SAXS measurement range ($0<q\leq6$ nm^{-1}), the atomic form factors are essentially equal to the atomic numbers Z_A and Z_B. This means the Laue monotonic scattering is independent of scattering angle in this small angle region. For the $Al_{1-x}Ga_x$ binary system, the Laue monotonic scattering intensity can be expressed as

$$I_{LM}(\text{random})=x(1-x)(Z_{Ga}-Z_{Al})^2 = 324x(1-x). \qquad (2.4)$$

The comparison between this simple theoretical expression and the experiments for various x can provide information on the alloy randomness. Deviations can be due to clustering, precipitation, or short range ordering [3].

2.1.2 Incoherent Compton Scattering

When we consider the scattered radiation from one bound electron, the total intensity scattered per electron (coherent+Compton) is given by the classical formula of Thomson. It can be written as the sum of elastic scattering (coherent scattering, I_{coh}) and inelastic scattering (incoherent Compton scattering, I_{inc}) [4]:

$$I_e=I_{coh}+I_{ic}. \qquad (2.5)$$

For the coherent scattering, the scattering power of the electron is f_e^2; i.e. the coherent scattering intensity is

$$I_{coh}=I_e f_e^2, \qquad (2.6)$$

where I_e is the intensity given by Thomson's formula and f_e is the scattering factor of one electron. From Eqs. 2.5 and 2.6, the incoherent Compton scattering can be written as

$$I_{ic}=I_e(1-f_e^2). \tag{2.7}$$

The scattering factor f_e is unity for q=0 and decreases with an increase in q, the decrease being more rapid if the electron wavefunction is more extended. Inversely, the incoherent Compton scattering is zero at q=0 and increases with q.

For a material consisting of a single element of atomic number Z, the incoherent Compton scattering can be written as

$$I_{ic}=I_e\sum_{j=1}^{Z}(1-f_{ej}^2)=I_e(Z-\sum_{j=1}^{Z}f_{ej}^2), \tag{2.8}$$

where f_{ej} is scattering factor for the jth electron. In Eq. 2.8, the second term is the atomic form factor,

$$f(q)=\sum_{j=1}^{Z}f_{ej}. \tag{2.9}$$

Therefore, the incoherent Compton intensity can be written in electron units as [4]

$$I_{ic}(eu) = \frac{I_{ic}}{I_e} = Z - f(q). \qquad (2.10)$$

Values of f(q) has been calculated for Al [4, 5, 6].

2.1.3 Thermal Diffuse Scattering (TDS)

The atoms of a solid vibrate with an amplitude which increases with temperature and does not become zero at the absolute zero of temperature because of the zero point energy. This atomic vibration of atoms, away from their equilibrium positions, is the origin of TDS.

For a monatomic solid, the TDS intensity can be written in the high temperature regime (equipartition limit) as [3]

$$I_{td}=\frac{f^2 k_B T}{m V_l^2}, \qquad (2.11)$$

where m is the mass of the atom, V_l is the longitudinal phonon velocity (transverse phonons do not participate due to the geometry of the SAXS measurement), and k_B is the

Boltzmann constant. In the small angle region, the atomic form factor f can be replaced by Z as mentioned in section 2.1.1. Therefore, Eq. 2.11 can be expressed as

$$I_{td}=\frac{Z^2k_BT}{mV_l^2}. \qquad (2.12)$$

As shown by Eq. 2.12, TDS has no q dependence in the region of the SAXS measurements. The numerical value of I_{td} for pure Al is 0.4 eu at room temperature [7].

2.1.4. Double Bragg Scattering (DBS)

Consider a sample composed of small crystallites and a ray reflected from one of these. When the reflected ray meets a second crystallite at the Bragg angle, it is again reflected. If the two crystallites are parallel, the doubly reflected ray emerges parallel to the incident ray. Double reflection can therefore give rise to small angle scattering.

When a metal is cold-worked, there is a considerable increase in the small angle intensity in the angular range of one or two degrees. This can be partly due to a reduction in grain size and introduction of strains extending the

intra-grain SAXS contribution out to larger angles. It also is due to cold work breaking up the larger grains into small sub-grains with slightly varying orientations. Then, the beam first reflected has a much higher probability of meeting suitably oriented grains for the second reflection than was the case for a sample in which neighboring grains have a completely random orientation.

Warren [8] reported the small angle intensity due to inter-grain multiple scattering from cold-worked copper with point-collimation SAXS geometry. The equation derived for the intensity due to DBS in electron units is valid for random grain orientations and was given as [8]

$$I_{DBS} \cong \frac{A}{q}, \text{ with} \qquad (2.13)$$

$$A = \frac{45\lambda^5 v_0}{16\pi^2 v_a^4 \mu} \sum_i \frac{m^2 f(\theta_i)^4 (1 + \cos^4 2\theta_i)}{\sin^4\theta_i \sin 2\theta_i} \{1 - \frac{(1 - e^{-g_i})}{g_i}\},$$

where m is the Bragg plane multiplicity, v_a is the unit cell volume, θ_i is the Bragg angle for the (hkl) reflection, g_i is $\frac{2\mu t \sin^2\theta_i}{\cos 2\theta_i}$, μ is the linear adsorption coefficient, t is the thickness of sample and v_0 is the volume per atom. From Eq. 2.13, the multiple scattering intensity can be estimated for pure polycrystalline aluminum. A is calculated to be

ARTHUR LAKES LIBRARY
COLORADO SCHOOL OF MINES
GOLDEN, CO 80401

1.84 eu/nm. Eq. 2.13, is valid for pinhole collimation. It is therefore necessary to smear the I_{DBS} calculated from Eq. 2.13 before applying it to the line-collimation system used here.

2.1.5 Dislocation Scattering

The small-angle signal has often been observed to vary as q^{-2} for a line collimation system in the range of q from about 10^{-2} to 1 nm^{-1}. One possible explanation of this behavior has been given [9] in terms of dislocations, in analogy to the case of crystalline materials [10, 11]. This behavior will be investigated for cold-worked Al.

2.2 Slit Collimation

An ideal SAXS apparatus would involve pinhole collimation with a high intensity X-ray source. Pinhole collimation allows the most straightforward inversion of the data to obtain the real space density fluctuation information. However, the intensity is limited in pinhole collimation, unless one takes advantage of synchrotron facilites [12]. Therefore, many experimental systems for SAXS, including the Kratky system used here, employ slit collimation in order to provide sufficient scattered intensity. As a result, the SAXS-determined intensity

contains various distortions. In order to convert such distorted intensities by slit collimation to ideal pinhole intensities, it is necessary to take into account smearing of the ideal curve profile. The slit width is the narrow dimension of the rectangular beam and its effect is negligible in most cases compared to slit length effect. As shown by several authors [18-22], the the slit length effect is important and depends on q. In this thesis, the higher q region is of importance and in order to examine the diffuse scattering an understanding of the slit smearing effect in this region is needed.

2.2.1 Beam Profile

In order to test the slit smearing of our line-collimation system, it is necessary to study the beam profile at the detector slit plane and its dependence on the dimensions of the detector slit. A slit length function F(x) represents the intensity profile versus position x in mm from the center of the detector slit. From F(x), the slit weighting function P(t) can be obtained and then used to calculate a smeared scattered intensity, J(q), from the pinhole intensity $I_p(q)$. The symbol t is the coordinate from the center of primary beam (at the detector slit) in the

direction of slit length but has been converted from x to the same units as q (nm^{-1}), i.e. [17]

$$t=\frac{2\pi x}{a\lambda}, \qquad (2.14)$$

where a is the distance between the sample and detector slit. The smearing is performed by integration [17]:

$$J(q)=\int_{-\infty}^{\infty} P(t)\, I_p(\sqrt{(q^2 + t^2)})dt \qquad (2.15)$$

P(t) will be determined from the experimentally measured F(x) profile. It is important to note that a diffuse component in I_p, due to its lack of a q dependence, should not be affected by the slit smearing integration shown in Eq. 2.15.

2.2.2 Two-Phase Model

Under suitable line-focus collimation, a useful invariant is given by [18]

$$Q = \frac{q_s}{2}\int_{0}^{\infty} q[J(q)]dq, \qquad (2.16)$$

where any diffuse component has been subtracted so only the microstructural component [Eq 2.1, where $J(q) \equiv I_M(q)$] is involved. The effective length of the primary beam, L, and the parameter q_s, which is defined as $\frac{2\pi L}{a\lambda}$, can both be determined from the slit length weighting function P(t). When a two-phase system is assumed, such as a sample which has a matrix of uniform electron density and precipitates with a different electron density, the relation between Q and the volume fraction of the precipitates, V_f, can be written [19]

$$Q = 2\pi^2 V_a (\Delta\rho)^2 V_f (1 - V_f), \qquad (2.17)$$

where $\Delta\rho = (\rho_m - \rho_p)$ is the electron density difference between matrix and precipitates.

2.2.3 Test of Infinite Slit Approximation

Equation 2.16 is valid for the so-called "infinite slit approximation" [20] and it is important to establish its range of validity for the actual finite slit length in the experiments. Combining Eqs. 2.15 and 2.16

$$Q=\frac{q_s}{2}\int_0^{\infty}\left[\int_{-\infty}^{\infty}P(t)I_p(\sqrt{q^2+t^2})dt\right]qdq. \quad (2.18)$$

For an infinite slit, the properly normalized P(t) will be given by $P(t)=1/q_S$ so that

$$Q_\infty = \int_0^{\infty}\int_0^{\infty} I_p(\sqrt{q^2+t^2})dtqdq, \quad (2.19)$$

while for a finite symmetric slit such that P(t)=0 for $|t| > t_{max}$

$$Q_{fin} = q_s\int_0^{\infty}\int_0^{t_{max}} P(t)I_p(\sqrt{q^2+t^2})dtqdq. \quad (2.20)$$

The validity of Eq 2.19 will be affected by the particle size of scattering sources of the SAXS. Assuming spherical particles, I_p can be approximated for our experimental q range by Gaussian function

$$I_p(q) = e^{-k^2q^2} \quad (2.21)$$

where $k^2=R^2/5$ and R is the sphere radius. Substitution into Eq. 2.19 yields $Q_\infty = \frac{\sqrt{\pi}}{4k^3}$. Once the function P(t) is determined for the experimental collimation system, a comparison can be made to the value of Q_{fin} from Eq. 2.20. This analysis should lead to the size limit on R for the validity of the infinite slit approximation for our SAXS system. Since the experimental range is only up to 6 nm^{-1} rather than ∞, the errors in Q will also need to be examined due to this limitation.

Chapter 3

Aluminum Gallium System

3.1 Aluminum-Gallium Binary Phase Diagram

According to most reports [21-24], gallium and aluminum form a simple eutectic system. The most recent Al-Ga phase diagram is provided by Murray [25] and is shown in figure 3.1. The eutectic is close to the Ga end of the diagram: 97 at.% Ga at 27.5°C (the melting temperature of Ga). Above the Ga melting temperature, numerical values of the solubility of Ga in fcc Al are shown in table 3.1 [25].

There is little data on lattice parameter versus Ga content of the solid solution phase. The lattice parameter of an alloy with 0.53 at.% Ga was found to be practically identical with that of pure aluminum (0.40494 nm) [26], but it increases to a value of 0.40504 nm at 0.64 at.% Ga [26], which gives a rough extrapolated value of 0.4057 nm at the solubility limit of 8.8 at.% Ga. The density also increases linearly to reach a value of 2.74 g/cm^3 at 1.02 at.% Ga [23].

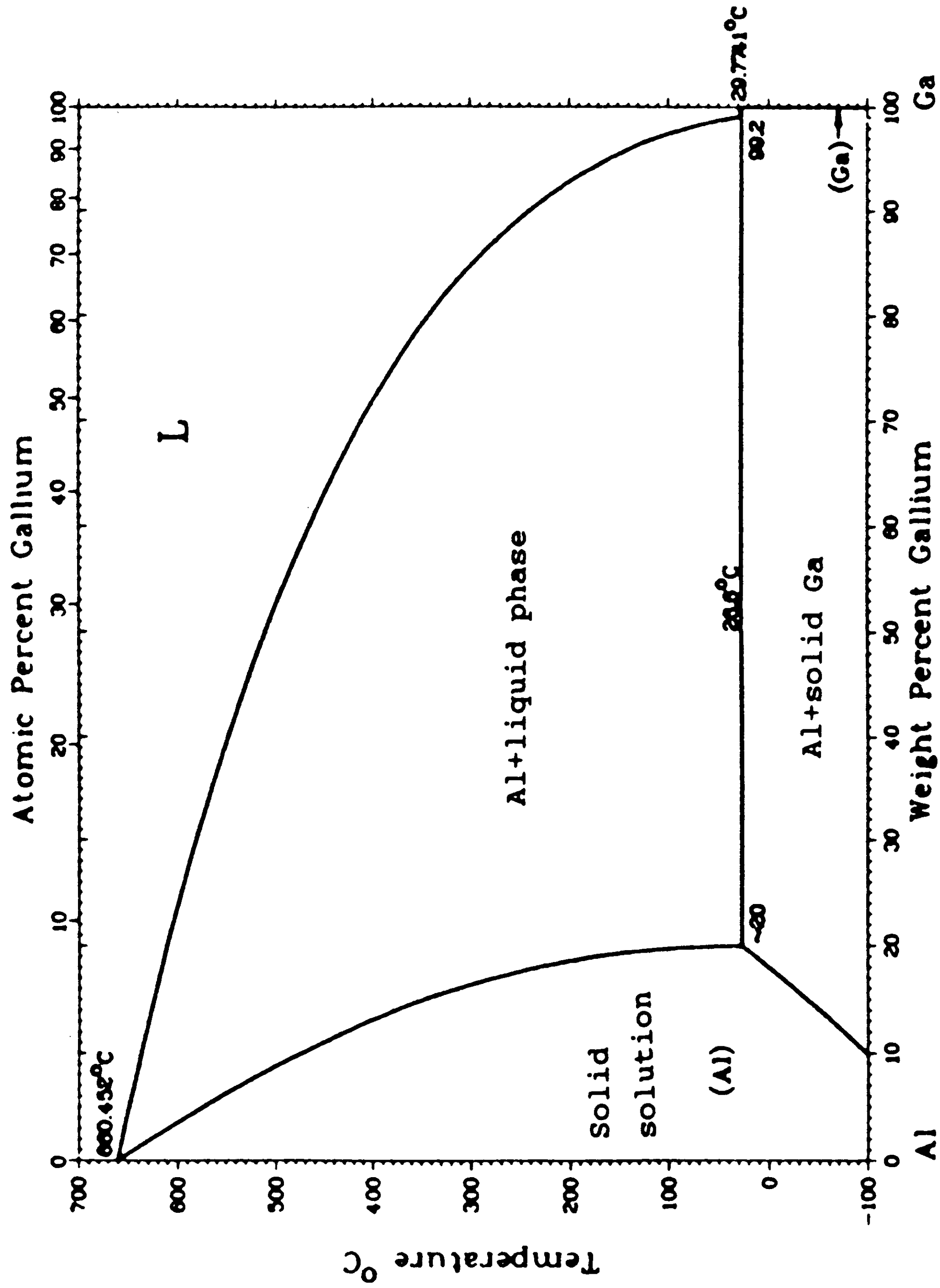

Figure 3.1 Aluminum gallium phase diagram by Murray[25].

Table 3.1 Equilibrium maximum solid solubility of Ga in Al for different temperatures (from the phase diagram of Murray [27].

T (℃)	150	200	250	300	350	400	500	550	600
C (wt.%)	20	19	18	17	16	15	13	10	6
C (at.%)	8.8	8.3	7.8	7.3	6.8	6.4	5.4	4.1	2.4

3.2 Diffusion of Ga in Al

When a melt composed of Al and Ga atoms is cooled to solidification, Ga and Al single crystal grains are formed during the cooling processes. In order to obtain a more random alloy, it is necessary to do proper heat treatment to enhance the diffusion mechanism and decrease the Ga precipitation. The diffusion of Ga in Al results from two distinct mechanisms: grain boundary diffusion and lattice diffusion. Grain boundary diffusion is the process of atomic transport due to a random jumping motion of the atoms along the highly disordered grain boundaries (as compared to adjacent grains) consisting of two-dimensional regions only a few atomic sizes in thickness (0.5 -1 nm).

Lattice diffusion is the process of atomic transport in the interior of the relatively defect-free, single crystal grains. The activation energy for the diffusion process along grain boundaries, in general, is much smaller, and therefore the atomic transport orders of magnitude faster than that of lattice diffusion. The grain boundary diffusion and lattice diffusion always occur at the same time, but lattice diffusion is the dominant term in the high temperature region, and grain boundary diffusion is dominant in the low temperature region [27, 28].

A mean penetration distance or diffusion length at some temperature and time X(t) is provided by solving Fick's law of diffusion [29].

$$X(t) = \sqrt{D(T)t} \tag{3.1}$$

where t is the time allowed for diffusion at temperature T, and D(T) is the diffusion coefficient at temperature T. In Eq. 3.1, D can be separated into D_b and D_l for grain boundary and lattice diffusion, respectively.

The relation between the diffusion coefficient and temperature had been investigated for Ga in Al [30, 31] and

a sensitive and unusual dependence of D_b and D_l on temperature has been observed. In this study, the goal is to prepare random $Al_{1-x}Ga_x$ alloys from melts composed of Al and Ga atoms. Thus we will consider only lattice diffusion of Ga into the relatively defect-free Al single crystal grains.

3.3 Lattice Diffusion of Gallium in Aluminum

The lattice diffusion coefficient D_l can be written as a function of temperature, and follows the traditional exponential law

$$D_l = D_0 \, e^{-E_a/k_B T}, \tag{3.2}$$

where E_a is the activation energy for the inter-diffusion of Ga atoms and Al atoms within the fcc lattice, k_B is Boltzmann's constant, and T is the temperature in Kelvin. Peterson and Rothman [31] studied the impurity diffusion of Ga in Al and reported

$$D_l \text{ (in cm}^2\text{/ s)} = 0.490 \exp[-1.2625 \text{ (eV)} / k_B T] \tag{3.3}$$

Based on this expression, the diffusion coefficients D_l at various temperatures are shown in table 3.2. A mean diffusion distance X(t) can be calculated from eq. 3.1. In order to estimate the time for complete lattice diffusion of whole grains, it is necessary to know the average grain size. For example, D_l is 1.5×10^{-10} cm^2/s at 400°C and assumming an average grain diameter of 20μm, then 7.4 hours are needed for Ga to diffuse from one side to the other. From these appropriate heat treatments can be designed to try to produce random alloys.

Table 3.2 Lattice diffusion coefficient of Ga in Al at various temperatures.

T (°C)	100	150	200	250	300	350	400	450	500	550
D_l (cm^2/s)	3.5×10^{-18}	3.7×10^{-16}	1.5×10^{-14}	2.9×10^{-13}	3.4×10^{-12}	2.6×10^{-11}	1.5×10^{-10}	7.0×10^{-10}	2.6×10^{-9}	8.3×10^{-9}

Chapter 4

Experiment

4.1 Description of Small Angle Scattering Equipment.

Figure 4.1 shows a schematic diagram of the Kratky SAXS system which consists of a slit collimating unit mounted in a vacuum chamber. The 12 kW, rotating Cu target, X-ray generator provides the source X-ray beam. Data are collected at pressures below 30 millitorr in order to minimize the air background scattering. The detector used is an Ar-Xe gas-filled proportional counter with a high efficiency of 90 % for CuKα radiation. With this detector, a low dark intensity (absence of X-ray beam) is measured (0.16/s). This low value is crucial for allowing studies of the weak diffuse scattering. This apparatus also gives high data reproducibility, which is demonstrated with routine tests of standard samples such as Lupolen (a polyethylene standard supplied by the manufacturer of the SAXS system). The wavelength of pure CuKα radiation is 0.15418 nm, which is selected by a graphite crystal monochromator mounted in front of the entrance slit. The slit settings for the system are: entrance slit width 130 μm, sample slit length 14 mm, and detector slit dimension 340 μm$\times$16 mm.

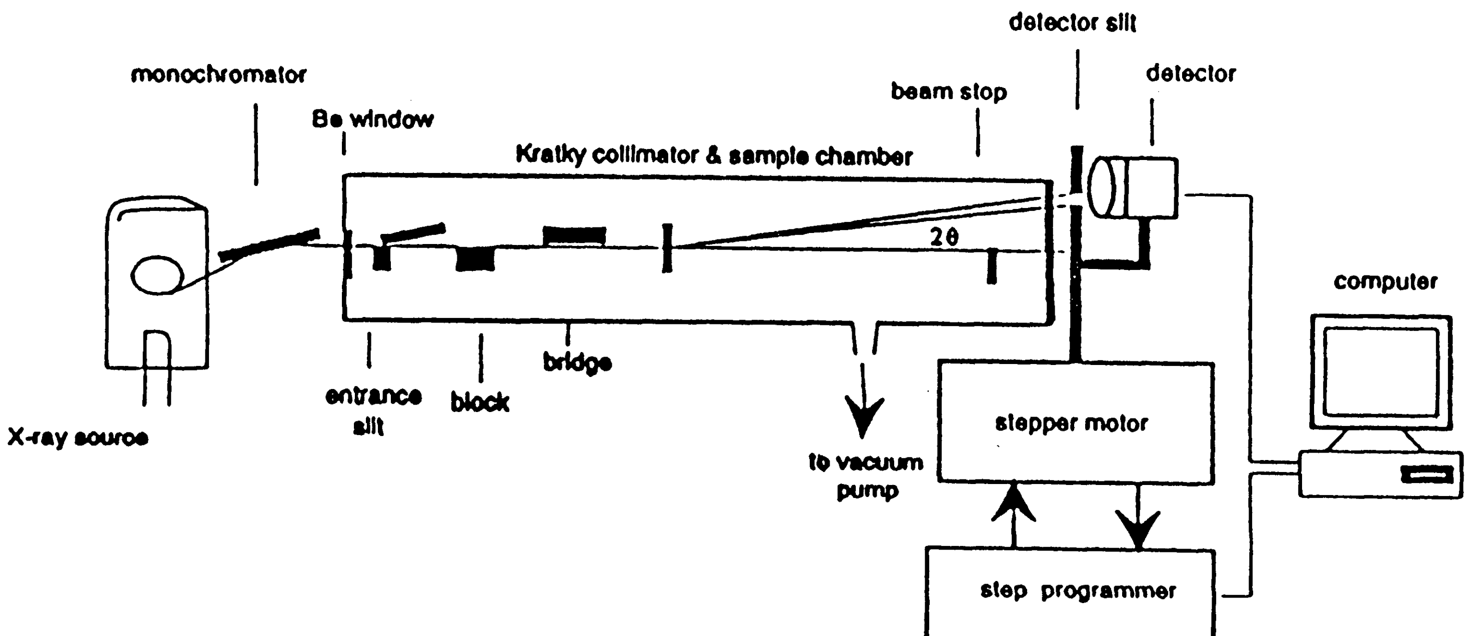

Figure 4.1 Schematic of SAXS system.

These experiment settings are considered a close approximation to the infinite slit setting of line-focus collimation [32]. Just how close is examined as part of this research. A stepper motor and step programmer drives the detector to predefined angles, and an IBM-PC controls the data collection. Usually a total measurement time is about 13 hours for collecting a data set of 120 points from 0.1 to 6 nm^{-1}.

4.2 Preparation of $Al_{1-x}Ga_x$ Alloys

A melting and step-cooling method was chosen to make a set of $Al_{1-x}Ga_x$ alloys with x=0, 0.025, 0.050, 0.070 and 0.100. The last composition exceeds the maximum solubility according to the phase diagram in Fig 3.1 so evidence of precipitation is expected. The preparation of $Al_{1-x}Ga_x$ alloys can be divided into the following steps.

i) Preparation of the pure Al and Ga.

ii) Melting and step-cooling or quenching

iii) Rolling into foils of suitable thickness.

iv) Annealing

4.2.1 Preparation of the Al and Ga

The purity of the starting Al and Ga was 99.999% and 99.9999%, respectively. Figure 4.2 shows the schematic

diagram for the pure Al block that has a hole on the center for mounting the Ga inside. Before inserting the pure Ga, it was necessary to remove the impurities on the surface and surface oxidization of the Al block and measure the exact weight ratio of Al and Ga to yield the selected alloy compositions given above.

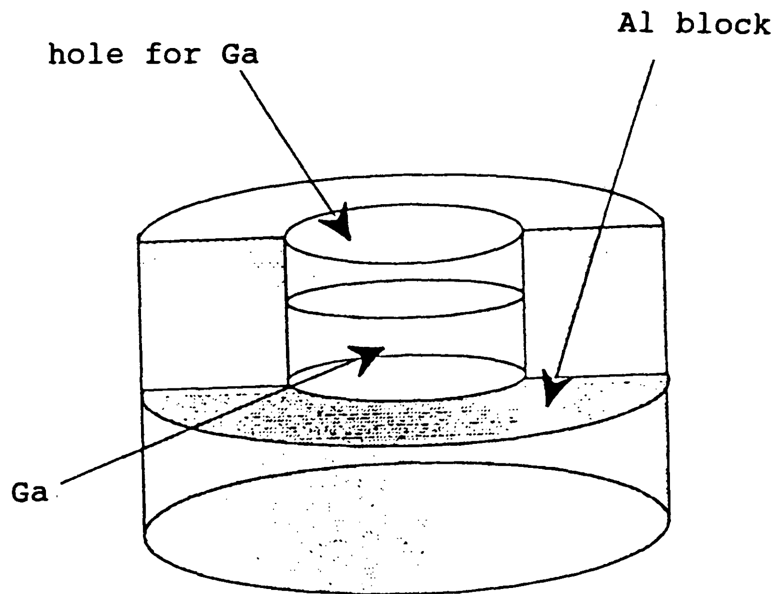

Figure 4.2 Schematic diagram of Ga inside of Al block.

Therefore, the Al block was etched in a NaOH solution (NaOH (1g)+DI-H_2O (100 ml)) for 5-6 min, then, washed for 10 min in DI-H_2O. After etching, the Al block was weighed to a precision of ±0.0003 g. The appropriate amount of Ga was then weighed to a similar precision for each alloy. Table 4.2.1 shows the amounts of Al and Ga for each alloy and the weight before and after melting. From this table, one can see there was no detectable loss of Ga and Al during the melting procedure.

Table 4.2.1. Mass of Al and Ga of each alloy and the total mass before and after melt

Sample	#2 x=0.025 (g)	#3 x=0.05 (g)	#4 x=0.07 (g)	#5 x=0.10 (g)
Al	0.8370	0.8205	0.9778	0.8633
Ga	0.0555	0.1116	0.1901	0.2478
Al+Ga (before melt)	0.8925	0.9321	1.1679	1.1111
Al+Ga (after melt)	0.8926	0.9320	1.1679	1.1111

* All values in the table have an uncertainty ±0.0003 g.

4.2.2 Melting and Step-cooling

Next, the samples prepared in the first step are melted in a tube furnace with programmable temperature control and step-cooled from 670°C to room temperature. In order to avoid surface oxidation of the samples during the melting and the cooling process, a graphite boat was specially designed for the samples. Figure 4.3 shows the graphite boat and tube furnace. Before pushing the graphite boat containing the samples into the high temperature zone of the furnace, the sealed tube was alternately evacuated and purged several times. A constant flow of high purity helium gas was then fixed at 4.5 SCFH. The sample was then pushed using the thermocouple rod into the furnace whose temperature was prestablized at 670°C. The Al and Ga metal mixture was left in the melted state for three hours to homogenize, then cooled to 450 °C at a rate of -10 °C/min. The sample was kept for 3 hours at 450 °C and then cooled to room temperatue at the rate of -0.4 °C/min in order to obtain the maximum solubility of Ga in Al (see Fig. 4.4 and Fig. 3.1).

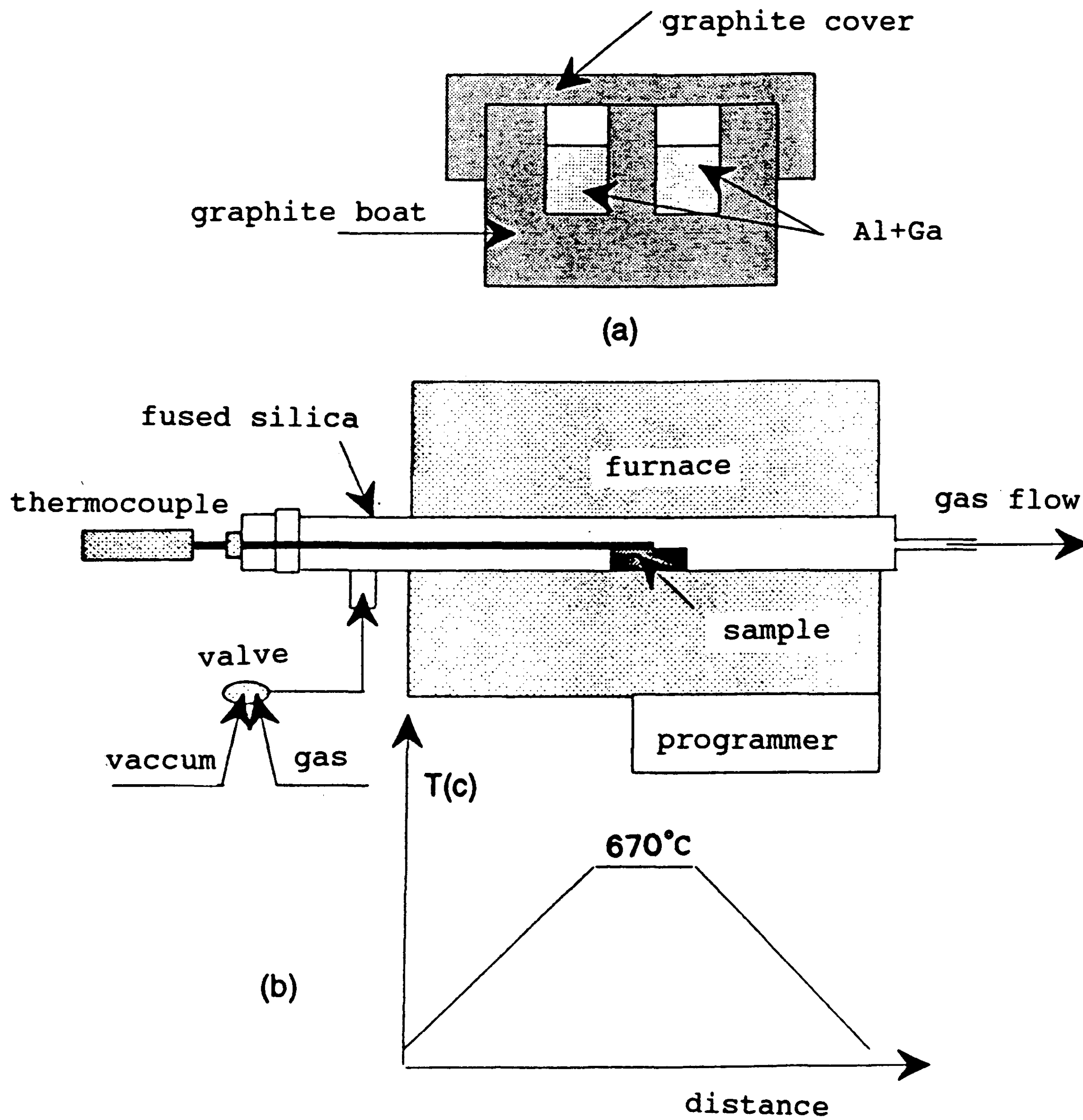

Figure 4.3 Schematic diagram of graphite boat (a) and furnace (b).

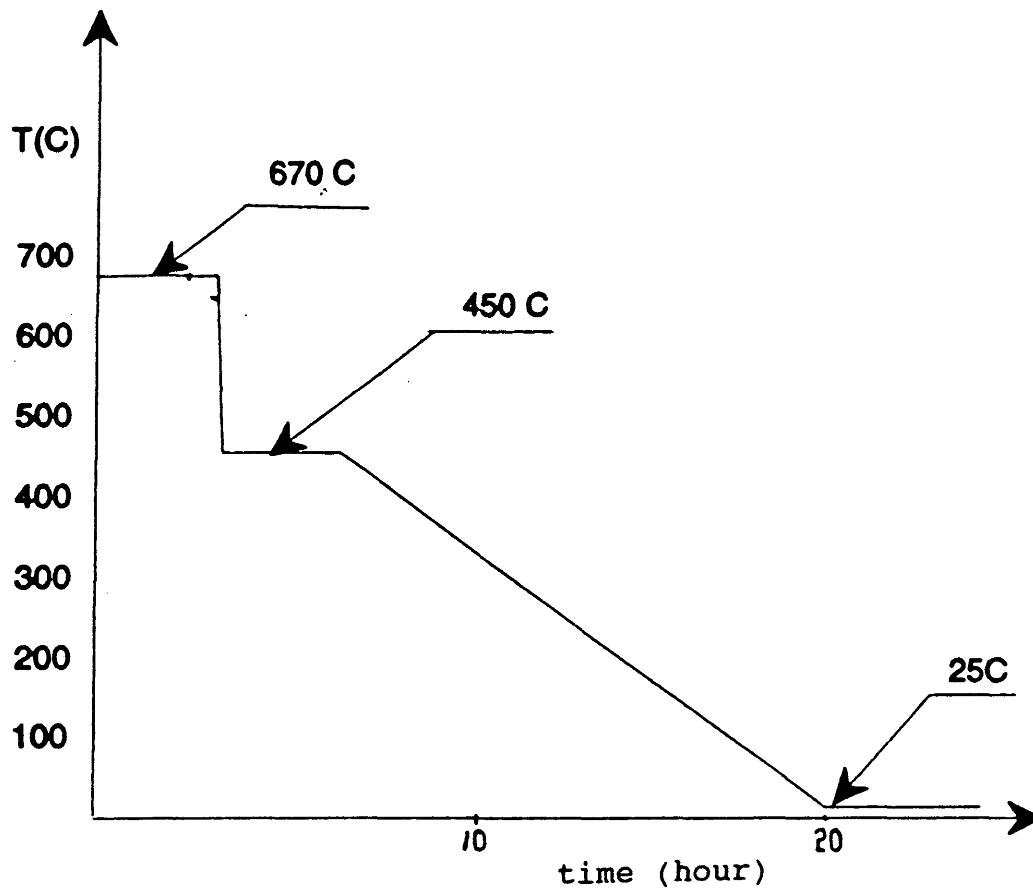

Figure 4.4 Melting and step cooling diagram of AlGa.

4.2.3 Sample Rolling and Heat Treatment

When the above two steps were completed, the SAXS samples were made into the form of foils by cold rolling. The sample thickness should be 70-75 μm, corresponding to about one absorption length of the Cu X-ray. This cold work procedure may leave the samples in a state of residual stress and lead to possible effects in the SAXS due to double Bragg scattering and dislocation scattering. Therefore, additional annealing was applied to one set of samples to reduce rolling damage, increase grain size and perhaps cause further homogenization of the solid solutions by lattice diffusion at high temperature. This set of samples was annealed at 400°C for 5 hours. All samples studied are listed in table 4.2.2. In the table, #1b, #2b, #3b, #4b, and #5b were used for checking the aging effect of lattice parameters after 80 days (#1ba, #2ba, #3ba, #4ba, and #5ba). These samples are the other pieces of #1a, #2a, #3a, #4a, and #5a respectively.

Table 4.2.2 Labels of $Al_{1-x}Ga_x$ alloys

	as-rolled (not annealed)		annealed (400x5hr)	aged (80 days)
Pure Aluminum	#1a	#1b	#1ah	#1ba
$Al_{0.975}Ga_{0.025}$	#2a	#2b	#2ah	#2ba
$Al_{0.95}Ga_{0.05}$	#3a	#3b	#3ah	#3ba
$Al_{0.93}Ga_{0.07}$	#4a	#4b	#4ah	#4ba
$Al_{0.9}Ga_{0.1}$	#5a	#5b	#5ah	#5ba

4.3 SAXS Data Reduction Procedures

4.3.1 Intensity Normalization

Most samples examined in the research at CSM are usually thin films deposited on a substrate and their thicknesses are different. Thus, in order to compare the SAXS data among different samples, a preliminary procedure is needed to subtract the substrate's contribution from a separate scan of the substrate only, correct for absorption, and normalize for the incident beam intensity. When the sample is not on a substrate, a scan is made with no sample in the chamber (blank scattering) to correct for scattering from the tail of the direct beam and parastic

scattering from the slit system. This can be treated the same as substrate scattering in the expression for normalized intensity [33]:

$$I_N(q) = \frac{[I_m(q) - I_d] - [I_s(q) - I_d]e^{-\mu_f t_f}}{P_o \mu_f t_f e^{-\mu_f t_f - \mu_s t_s}}, \qquad (4.1)$$

where the quantities in the above equation are defined as follows:

I_m= measured intensity from film+substrate.

I_s= measured intensity from substrate only.

I_d= dark background count rate (0.16/s).

μ_f, μ_s =linear absorption coefficients of film and substrate.

t_f, t_s =thickness of film and substrate.

P_o= incident intensity with no sample mounted and measured by moving slit method [34] just before a scan begins.

Using measurable quantities, the above equation can be rewritten as

$$I_N(q) = \frac{[I_m(q) - I_d] - [I_s(q) - I_d]\frac{P_f}{P_s}}{P_{f+s}\ln(\frac{P_s}{P_{f+s}})} \qquad (4.2)$$

where P_{f+s} and P_s represent the incident intensity (also measured by the moving-slit method) with sample (film+substrate) or substrate, respectively. For the case of a sample in the form of a foil, like the $Al_{1-x}Ga_x$ alloys of interest here, $I_s(q)$ is replaced by the data from the blank scan and P_{s+f} by P_f. Analysis is handled by a computer program.

4.3.2 Conversion of Normalized Intensity to Absolute Units.

In order to directly compare theoretical and experimental values, it is necessary to convert $I_N(q)$ into absolute units, known as electron units (eu) or electrons/atom (e/a). The conversion equation can be written as [1]:

$$J(q) = I_N(q)\left[\frac{\mu V_a a}{I_e A}\right] \tag{4.3}$$

where

$J(q)$ = intensity in electron units (electrons/atom)

V_a =average atomic volume of the sample

A = area of the detector slit

a = distance between sample and detector slit

I_e(Thomson cross section of electron)= 7.94×10^{-26} cm^2

μ= linear adsorption coefficient of sample (cm^{-1})

which can be found as follows:

$$\mu = (\sum_i [(\frac{\mu}{d})_i w_i])d_{sam}$$

$(\frac{\mu}{d})_i$ = mass absorption coefficient of element i in sample.

w_i= weight fraction of element i in sample, and

d_{sam}= mass density of sample.

For the SAXS system used here, A=0.0544 cm^2 and a=20 cm.

4.4 Measurement of the Slit Function F(x)

In order to understand the slit smearing effect, the slit length function F(x) and the associated weighting function P(t) defined in the previous chapter need to be found. The measurement of F(x) was made by recording the intensities at the detector plane through a 30 μm slit in 1 mm steps along x. F(x) was then fitted by a polynomial to provide a smooth function and establish the effective length of the beam, L, and the slit parameter q_s. This function was then convoluted with the detector slit, a step function 16 mm in length, and normalized. This normalized, convoluted beam profile, is then P(t).

4.5 Test of slit Smearing of Lupolen

For this test, a standard polyethylene sample (Lupolen) was used. A comparison is made between SAXS data obtained at CSM (line collimation) and a set of SAXS data (pinhole collimation) which was obtained at the Oak Ridge National Laboratory (ORNL) using the same standard polyethylene sample. The ORNL data were smeared via eq. 2.15 using the P(t) determined by the method in section 4.4.

4.6 X-ray Diffraction (XRD)

The structure and lattice parameters of the $Al_{1-x}Ga_x$ alloys were carefully investigated by XRD. The XRD experiments were done on the as-rolled series, annealed series and aged series as listed in table 4.2.2.

To obtain the XRD data, an IBM PC data collection system attached to a Rigaku X-ray diffraction unit was used. The X-ray source of this system is the same as mentioned in section 4.1. The intensities (counts/s) were recorded by the IBM computer as the angle 2θ increases in a step-wise manner. The XRD data (intensity versus 2θ), were fitted by a program to obtain the exact peak positions for each alloy. The finding of exact positions of peaks is

critical to calculate lattice parameters. For the calculation of the lattice parameter of each alloy, the $\frac{\cos^2\theta}{\sin\theta}$ extrapolation method was used as described in reference [35]. The main idea of this method can be described as follows.

i) Calculate the lattice constant a for each line,

ii) Plot the several values of a versus $\frac{\cos^2\theta}{\sin\theta}$, which should be linear, and the intercept at $\frac{\cos^2\theta}{\sin\theta}=0$ provides the lattice parameter of the sample.

Chapter 5

Results

5.1 Slit Smearing

5.1.1 Slit Length Weighting Function

Figure 5.1a shows the original beam profile F(x) and convoluted profile F'(x') of the Kratky system and Fig. 5.1b shows the weighting function P(t) obtained from F'(x') using Eq. 2.14. The original profile F(x) was normalized to unity at x=0 and convoluted with a rectangular step function representing the 16 mm wide detector slit. In Fig. 5.1a, DS represents detector slit and SS represents sample slit. The convolution integral can be written

$$F'(x') = \int_{-\infty}^{\infty} F(x)F(x - x')dx \qquad (-16 \le x' \le 16 \text{ mm}). \qquad (5.1)$$

Fitting with a polynomial yields

$$\begin{aligned} F'(x') = {} & 0.974 - 7.297 \times 10^{-4} x' - 3.669 \times 10^{-3} x'^2 \\ & + 1.717 \times 10^{-6} x'^3 + 4.408 \times 10^{-6} x'^4 \\ & - 8.965 \times 10^{-10} x'^5 - 1.638 \times 10^{-9} x'^6 \\ & (-19 \le x' \le 19 \text{ mm}). \end{aligned} \qquad (5.2)$$

From Eq. 5.1 and Eq. 2.14, the slit weighting function P(t) can be written as

$$P(t) = 0.974 - 3.578 \times 10^{-3} t - 8.943 \times 10^{-2} t^2 + 2.025 \times 10^{-4} t^3 + 2.549 \times 10^{-3} t^4 - 2.542 \times 10^{-6} t^5 - 2.277 \times 10^{-5} t^6 \quad (-5.3 \le t \le 5.3 \ \text{nm}^{-1}) \qquad (5.3)$$

Figure 5.1a shows a good agreement between data points and line fits of the original and convoluted profiles by polynomials. From Eqs. 5.2 and 5.3, the effective width of the primary beam L and the value of q_s can be found. L is 24±1 mm which is the rectangular width (area/height). The q_s can be determined by using the formula

$$q_s = \frac{2\pi L}{a\lambda}. \qquad (5.4)$$

Its numerical value is 4.9±0.2 nm^{-1} and the uncertainty is due to the uncertainty of L which came from the determination of the area under F(x) curve from the data points.

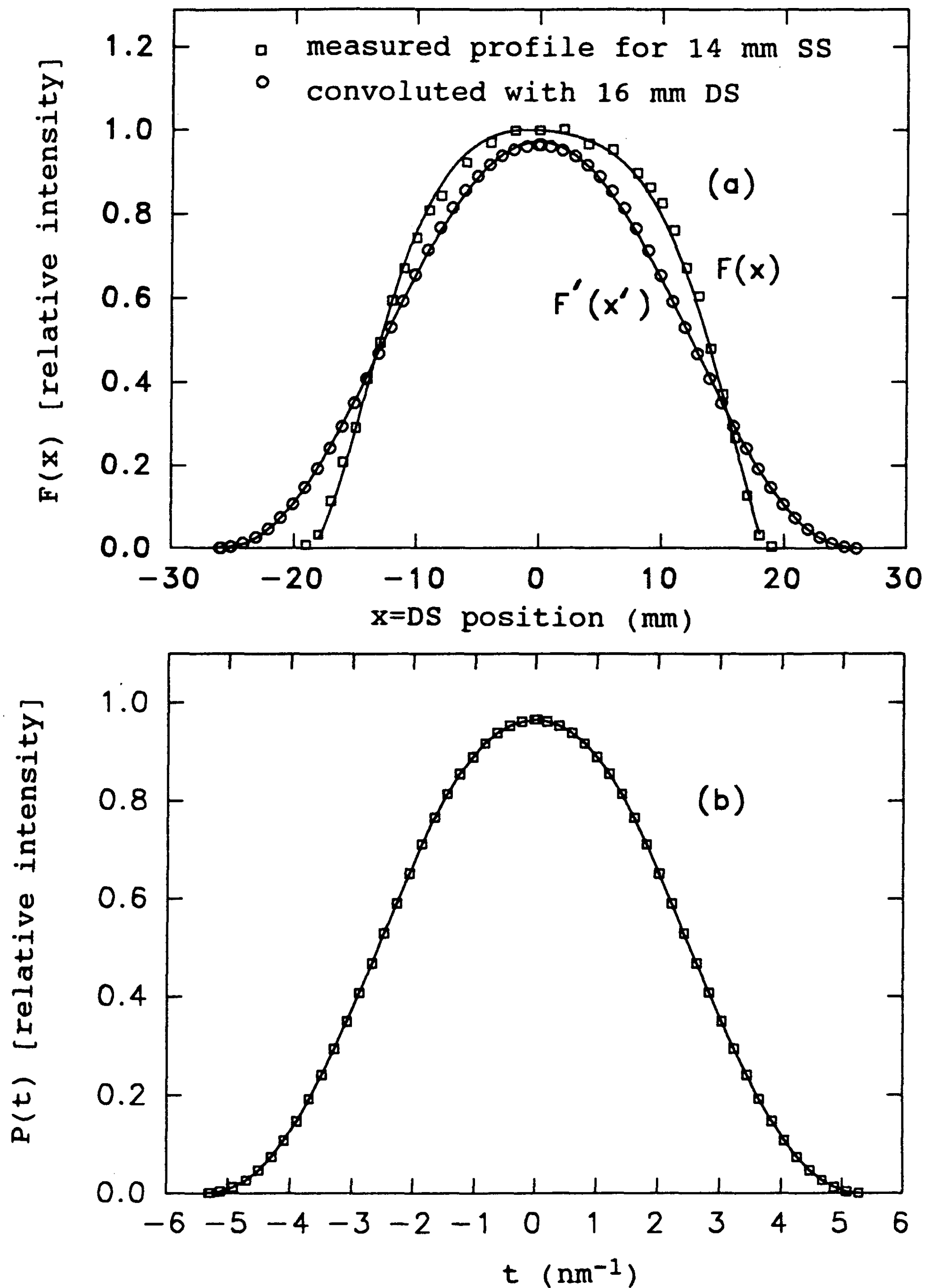

Figure 5.1 Results of beam profiles.
(a) shows F(x) and F'(x') which is convoluted from fitted function F(x). (b) shows the P(t) which ia a transform of F'(x').

5.1.2 Smearing Test Using P(t)

In order to compare the line-collimation data and point-focus ORNL data, the latter are smeared using Eq. 2.15 and the experimental P(t), Eq. 5.3. The results are plotted in Fig. 5.2. The units used in this case are the scattering cross section per unit volume (cm^{-1}) since a value for the volume per atom is not known for this polyethylene material. This figure shows the strong slit smearing effect in the low q region, but the CSM data and the ORNL data agree well at high q ($q \geq 2$ nm^{-1}) as expected for nearly q-independent intensity.

The solid line passing through the CSM data is the result of smearing the ORNL data, thereby demonstrating the use of Eq. 2.15 and the validity of the slit weighting function, Eq. 5.3.

5.1.3 Infinite Slit Approximation

Q_∞ and Q_{fin} were calculated from Eqs. 2.19-21 with the P(t) in Eq. 5.3. Figure 5.3 shows the ratio $\frac{Q_{fin}}{Q_\infty}$ versus the radius R of a spherical particle. In the figure, the filled circles show the ratio when P(t) is the experimental function given by Eq. 5.3. For P(t)=Eq. 5.3, there is negligible error for $R \geq 6$ nm, about 6% error for R=2 nm, and

about 20% error for R=1 nm. Thus one will underestimate the volume fraction of the second phase (via Eqs.2.16 and 2.17) if the particle size is very small.

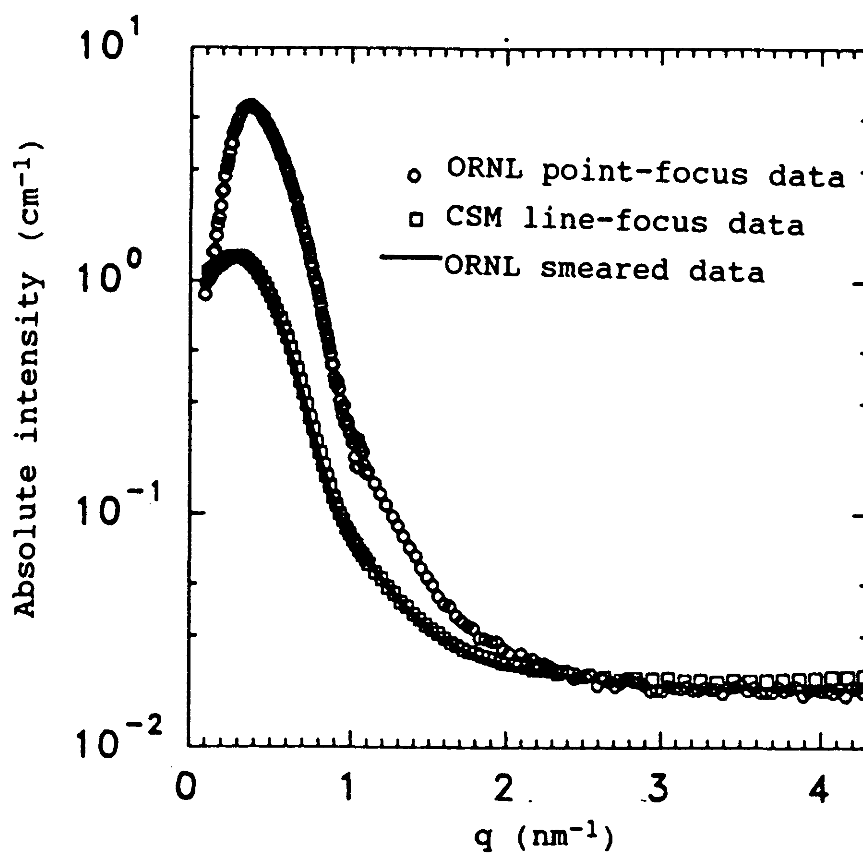

Figure 5.2 The result of slit smearing effect of standard polyethylene sample (lupolen).

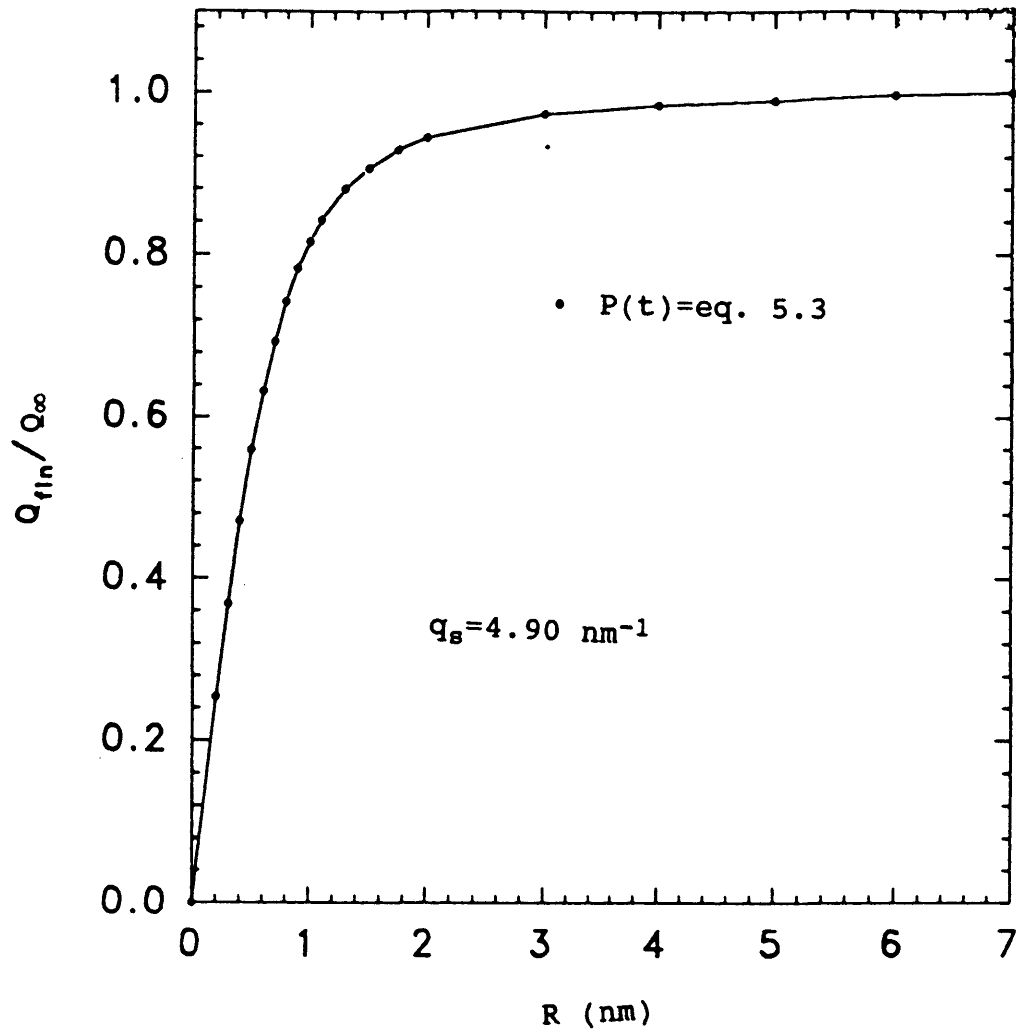

Figure 5.3 Ratio Q_{fin}/Q_{∞} versus radius of particle R.

5.2 Pure Al Scattering Mechanisms

Figure 5.4 shows the experimental SAXS data from the pure Al sample (#1a) and the various contributions expected from addition of DBS, TDS, and incoherent Compton scattering calculated for pure Al. The DBS, TDS and incoherent Compton scattering are theoretical results from Eqs. 2.10, 2.12, and 2.13. The DBS term was smeared by using Eq.2.15. The experimental data and the addition of I_{ic}, I_{DBS} and I_{td} agree well in the high q region, but they do not agree well in the low q region. The agreement at high q shows we have correctly accounted for all the diffuse scattering mechanisms. The disagreement at low q is probably due to surface roughness and dislocation scattering. The surface roughness effect is proportional to q^{-3} if the roughness scale is greater than π / q_{min} and dislocation scattering is proportional to q^{-2} in the case of line collimation [36-38]. Figure 5.5 shows the pure Al scattering after subtraction of I_{td}, I_{DBS} and I_{ic} on a log-log plot. The dotted line was least square fitted and its slope is -2.35. Its intermediate value between 2 and 3 suggests a mixture of dislocation and surface roughness scattering.

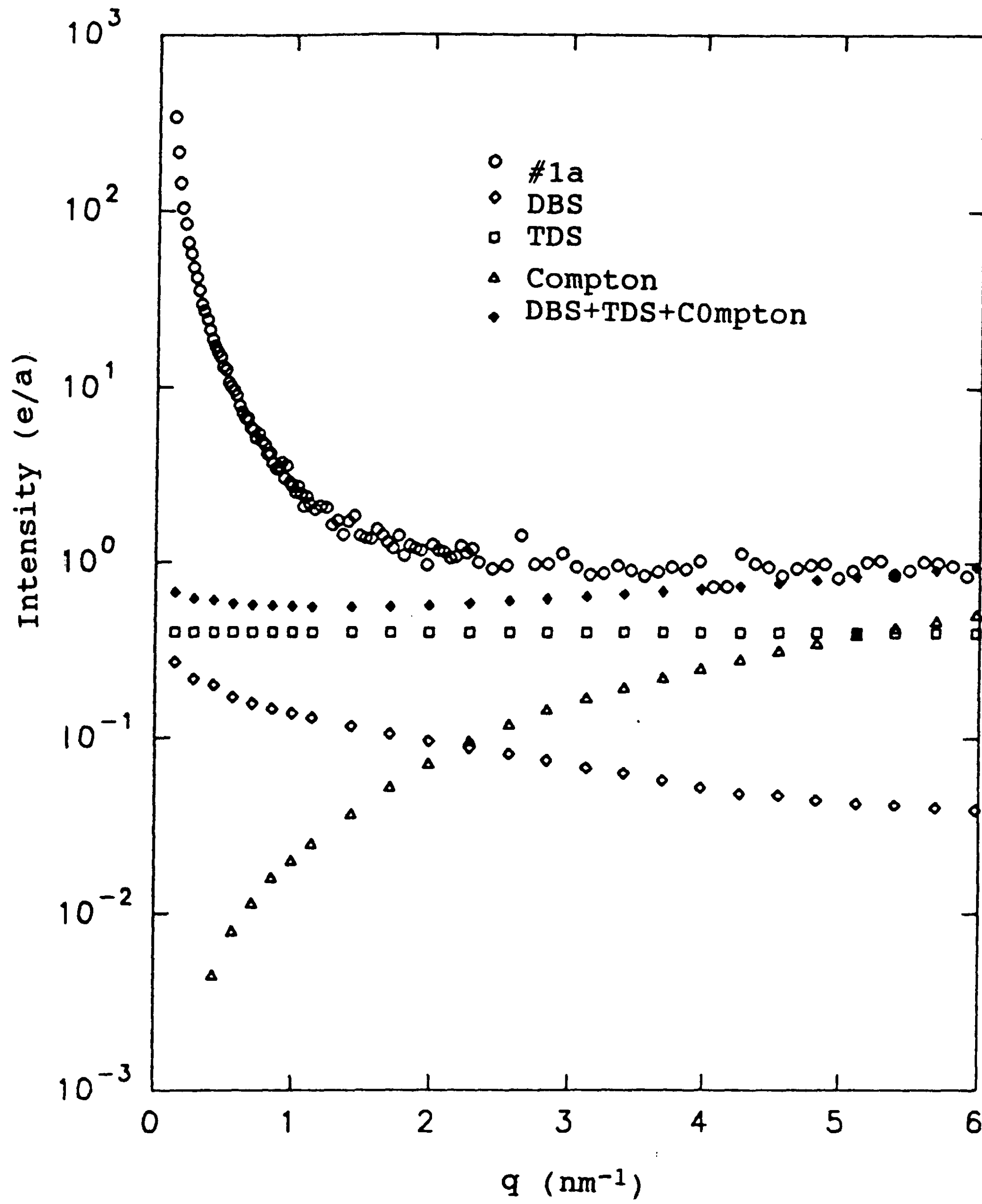

Figure 5.4 SAXS data from pure Al sample #1a and various theoretical contributions.

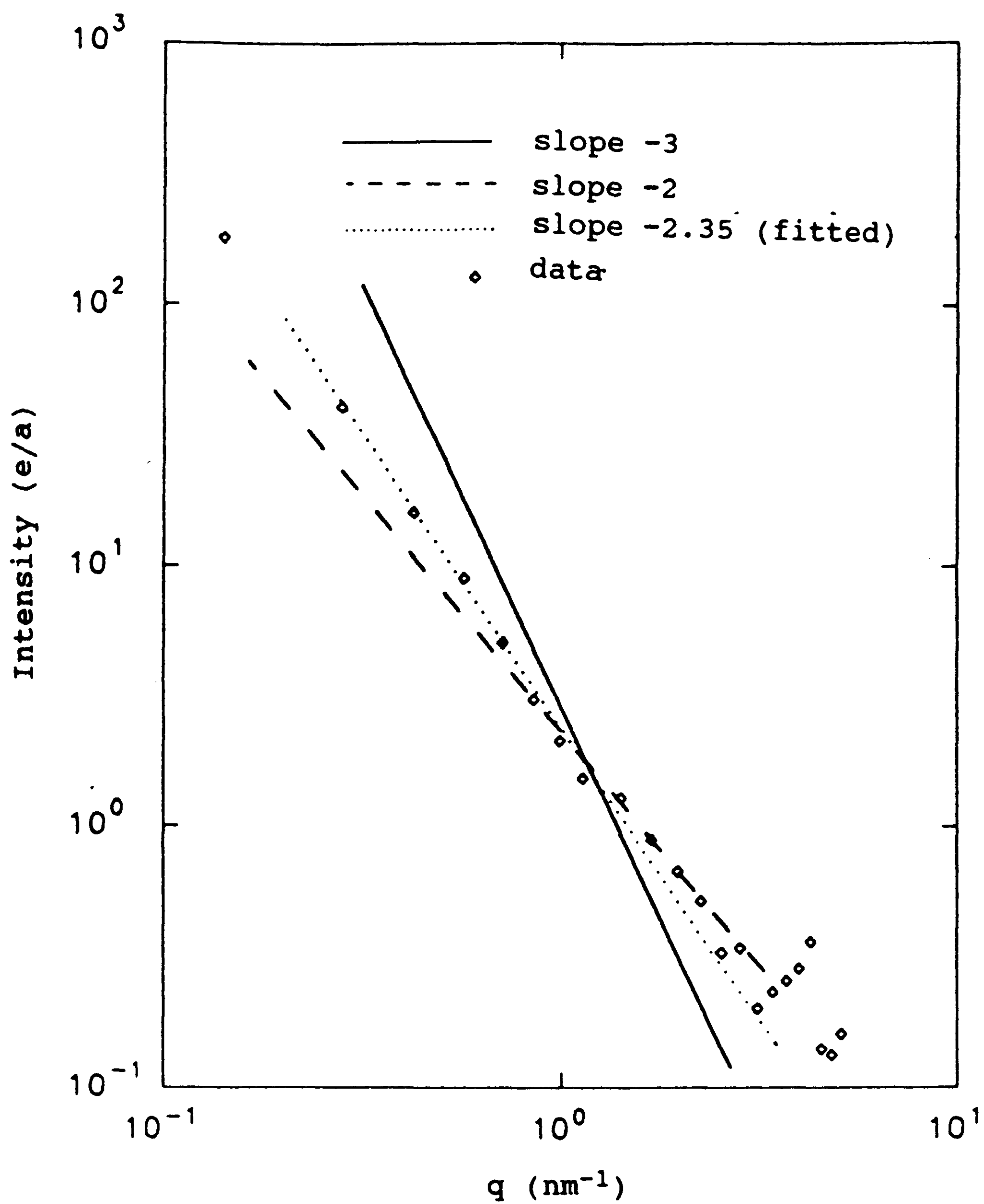

Figure 5.5 Pure Al SAXS data after subtraction of $I_{td}+I_{DBS}+I_{ic}$

5.3 $Al_{1-x}Ga_x$ Alloys

5.3.1 X-ray Diffraction (XRD)

Figure 5.6 shows the XRD results for the as-rolled series of alloys. There is no evidence of Ga peaks in the figure. However, as x increases, the relative amplitudes of the peaks change and their positions also slightly change. This means that the structure of the as-rolled $Al_{1-x}Ga_x$ alloys is single phase as detected by XRD (fcc), and the fcc lattice parameter increases slightly with Ga content. The differences in relative intensities are due to different rolling-induced textures. Figure 5.7 shows the change of the lattice parameter with x. In the figure, a_1 represents the fit of the lattice parameter just after the cold-work (series a in table 4.2.2) and a_2 shows the fit of the lattice parameter after the alloys were annealed at 400 °C for 5 hours (series ah in table 4.2.2). When the sample is reduced in thickness by rolling, a residual stress may remain and partial recovery may occur, even at room temperature [28]. Another set of XRD data was acquired after aging the a series for 80 days at room temperature and these are included in Fig. 5.7. These data suggest an approximately uniform drop in the lattice parameter for all the alloys.

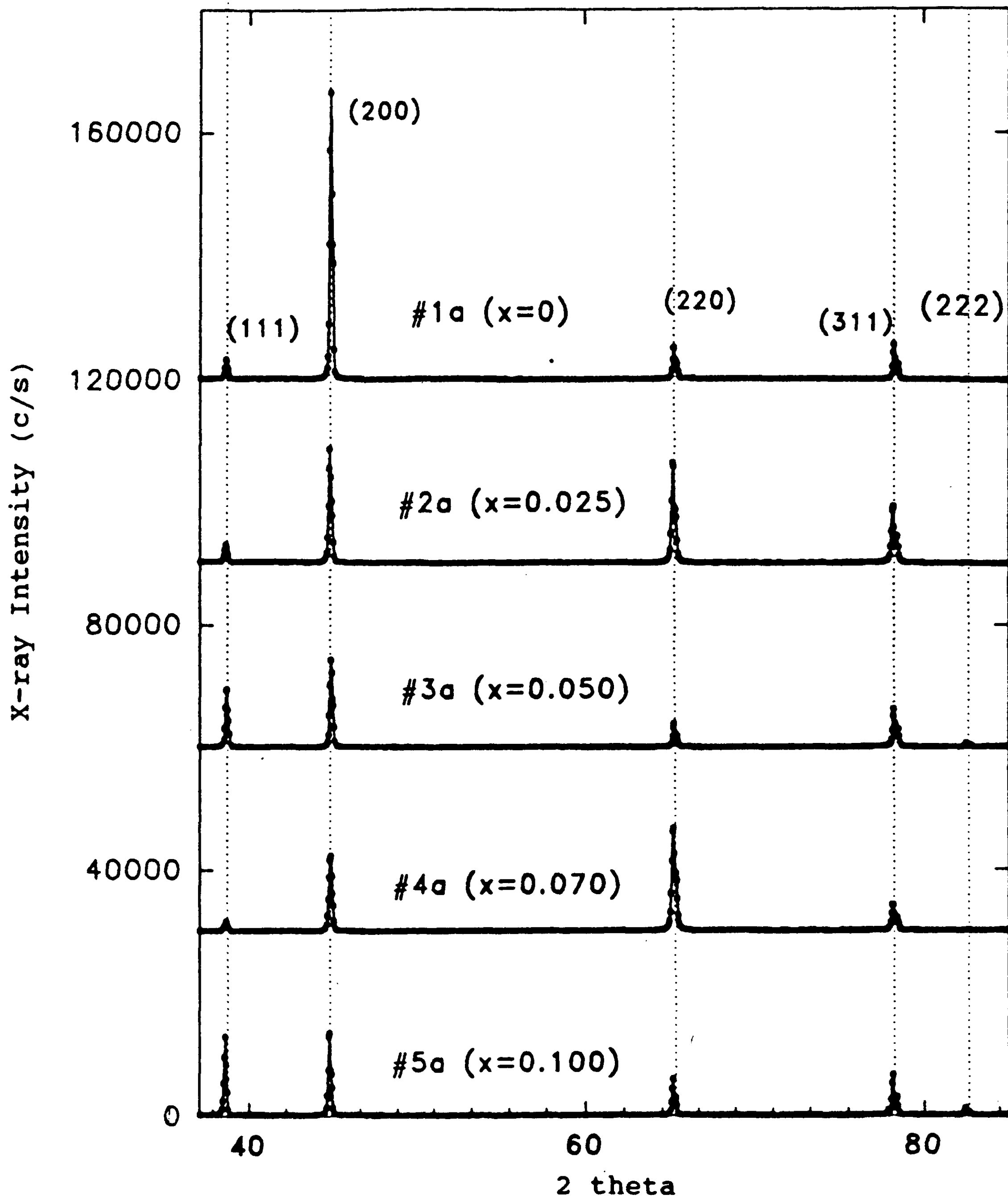

Figure 5.6 X-ray diffraction data from as-rolled $Al_{1-x}Ga_x$ alloys. Vertical dotted lines show the Bragg 2 theta values for pure Al.

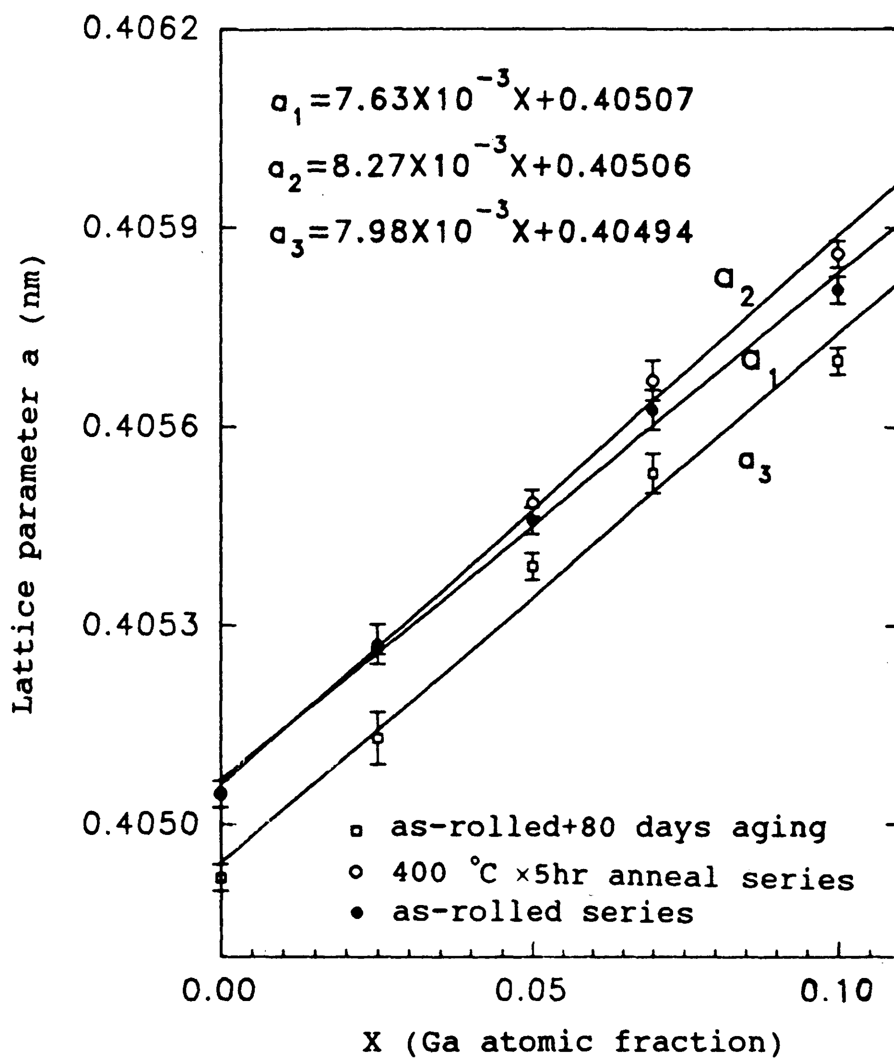

Figure 5.7 Alloy lattice parameter versus Ga atomic fraction x. a_1 is the line fit of as-rolled series. a_2 is the fit of annealed series. a_3 is the fit of as-rolled+80 days aging series.

Table 5.1 lists the experimental lattice parameters and Ga atomic fractions for samples studied. When the as-rolled samples are aged at room temperature, a residual compressive stress in the plane of the foil was apparently released such that the lattice parameter of pure Al (0.40494(2) nm) is the same as 0.40494 nm which was reported in JCPDS file [39].

ARTHUR LAKES LIBRARY
COLORADO SCHOOL OF MINES
GOLDEN, CO 80401

Table 5.1 The change of lattice parameters with x increase just after the cold-work and the annealing (400°C ×5 hr), and aged samples.

Sample	#1a (#1ah) [#1ba]	#2a (#2ah) [#2ba]	#3a (#3ah) [#3ba]	#4a (#4ah) [#3ba]	#5a (#5ah) [#ba]
x (atomic fraction)	0.0000	0.0250	0.0500	0.0700	0.1000
a (nm)	0.4050(2) (0.4050(2)) [0.40492(2)]	0.40525(3) (0.40525(1)) [0.40511(3)]	0.40540(1) (0.40542(2)) [0.40539(2)]	0.40561(3) (0.40566(2)) [0.40553(4)]	0.40581(2) (0.40586(3)) [0.40572(2)]

5.3.2 SAXS Results for $Al_{1-x}Ga_x$ Alloys

In order to examine the Ga alloy scattering effect in $Al_{1-x}Ga_x$ films, the separation of Laue monatomic scattering, I_{LM}, from the measured SAXS intensities is needed. As discussed in chapter 2, the measured intensity consists of the addition of all diffuse scattering mechanisms such as TDS, incoherent Compton scattering, I_{LM}, and other scattering mechanisms due to the surface roughness, dislocations, DBS, and electron density fluctuations in the sample (microstructure). If the pure Al contribution is subtracted and it is assumed that the TDS, DBS, Compton scattering, surface roughness and dislocation scattering are independent of x then the measured intensity after this subtraction has only two components, I_{LM} due to Ga alloying and scattering from microstructure, which is probably due to Ga precipitation.

Figure 5.8 (as-rolled) and Figure 5.9 (annealed) show the SAXS results of $Al_{1-x}Ga_x$ alloys. The dashed lines in Fig. 5.8b and Fig. 5.9b indicate the alloy scattering intensities. These lines were determined by fitting the data points in the range $4 \leq q \leq 6$ nm^{-1} after subtraction of the pure Al contribution from the alloys.

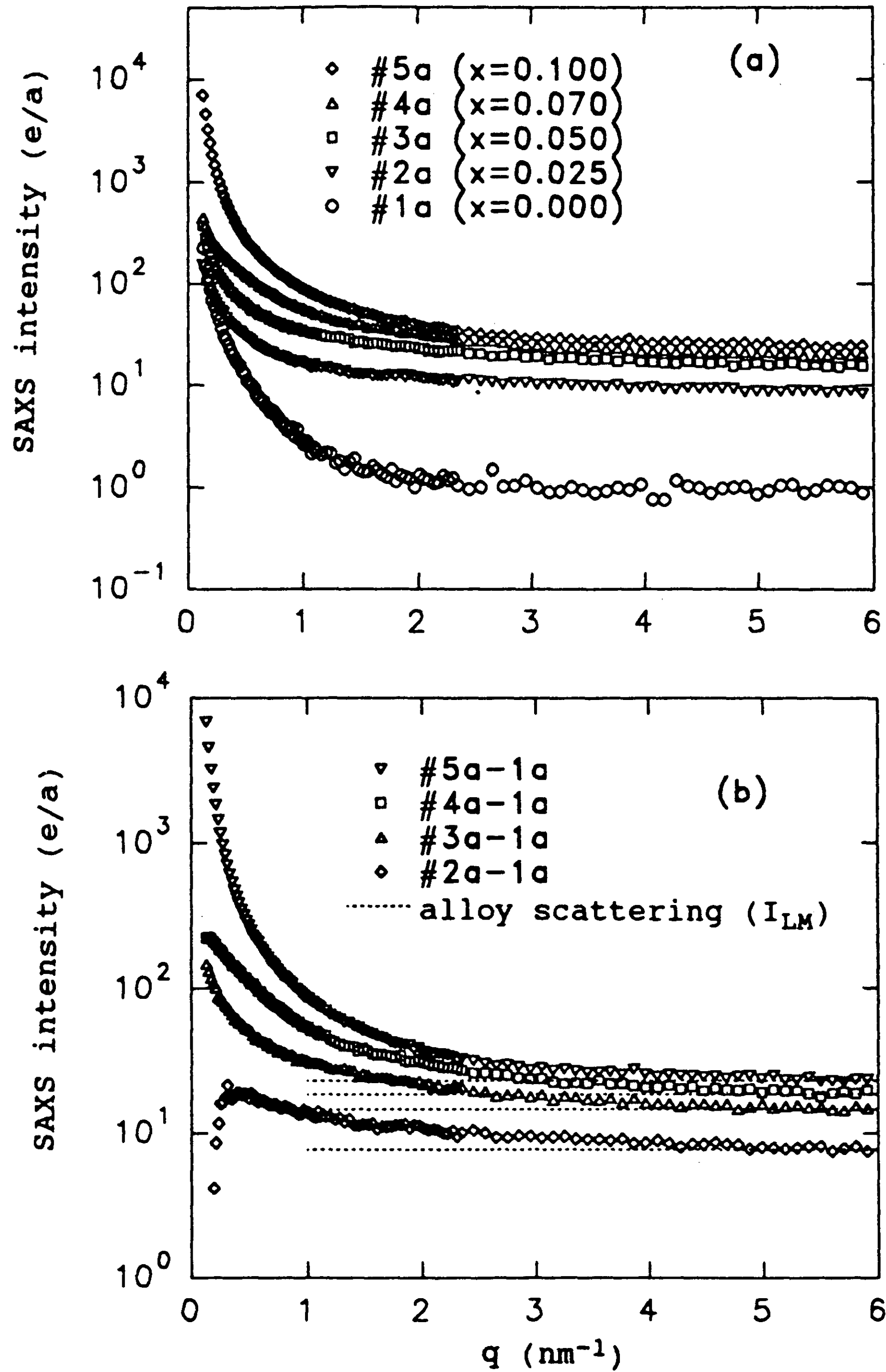

Figure 5.8 (a) SAXS intensity of as-rolled series
(b) SAXS intensity after subtraction of pure Al (#1a).

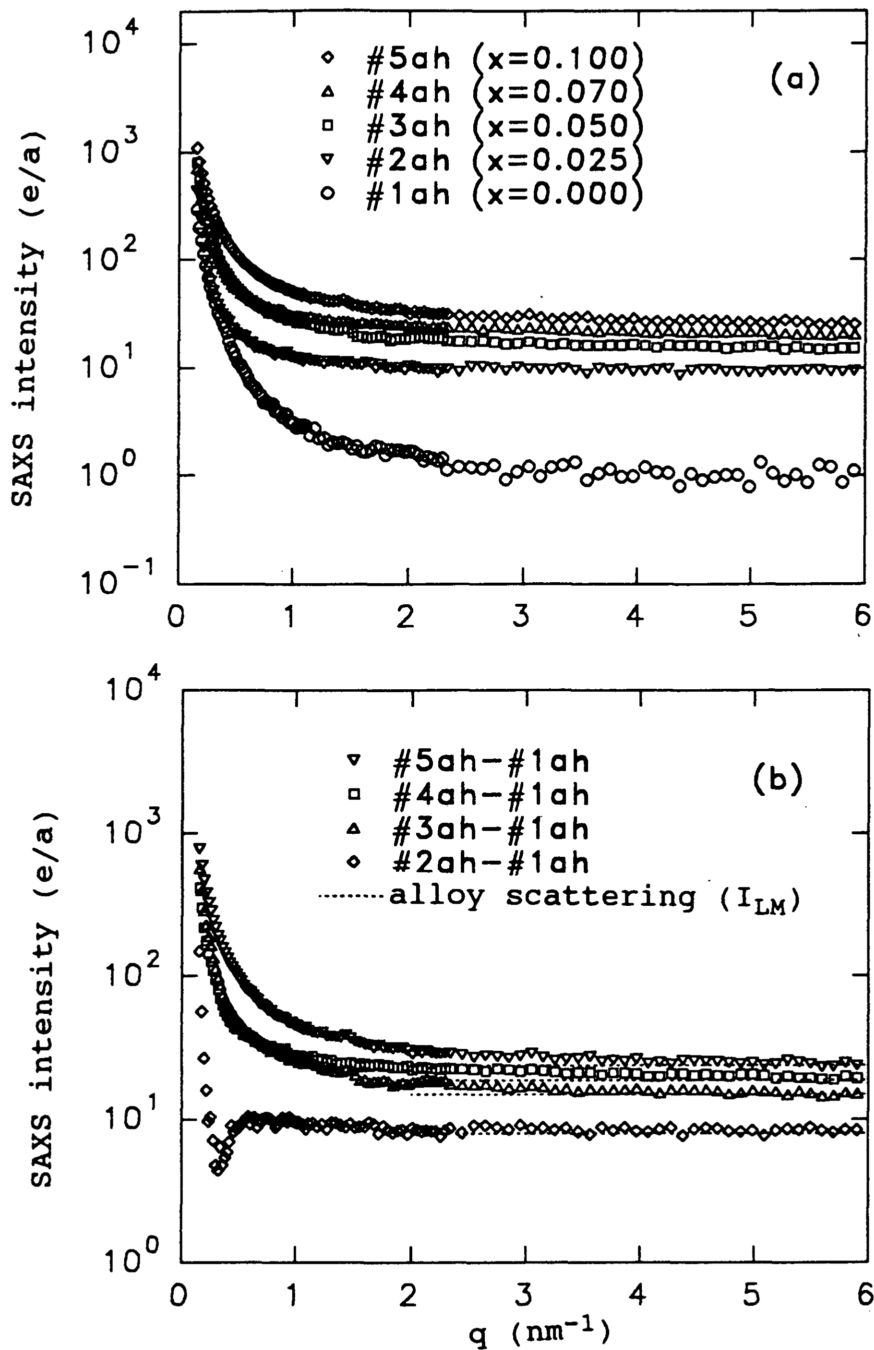

Figure 5.9 (a) SAXS intensity of annealed series.
(b) SAXS intensity after subtraction of pure Al (#1a).

The figures suggest alloys #2a and #2ah are almost perfectly random (intensity is almost constant), but other samples as-rolled #3a, #4a, #5a and annealed #3ah, #4ah, #5ah show the sharp increases of SAXS intensities in the small q regions. These are probably due to Ga clustering and precipitation based on the phase diagram in Fig. 3.1. This contribution due to Ga precipitation is negligible in the large q region compared to the alloy diffuse scattering intensity.

In the two-phase model (see section 2.2.2), the volume fraction of the second phase, V_f, can be calculated from Eq. 2.17 using the experimental Q value (Eq. 2.16), where the second phase is most likely Ga precipitates according to the phase diagram (Fig. 3.1). Table 5.2 shows the Q values (Al contribution to Q is subtracted) and volume fraction for each alloy. The V_f's in table 5.2 indicate a clear increase in the Ga precipitation with increases in Ga content. They also suggest that the annealed series [ah] has less precipitation. However, this may not be true for the following reason. If the Ga precipitates are large (>30 nm) then their primary SAXS intensity will be below the experimental q range and they will not be seen by SAXS except for the "tail" scattering which should vary as q^{-3}.[40]. The comparison of the experimental and theoretical

values of I_{LM} allows another method of determining the amount of Ga precipitation.

Table 5.2 Volume fractions and Q values for each alloy.

Sample	#2a [#2ah] x=0.025	#3a [#3ah] x=0.050	#4a [#4ah] x=0.070	#5a [#5ah] x=0.100
Q (eu/nm^3)	46(3) [10(2)]	135(9) [95(8)]	251(14) [110(10)]	589(26) [181(9)]
V_f (%)	0.024(2) [0.005(1)]	0.075(4) [0.053(4)]	0.147(6) [0.065(5)]	0.380(8) [0.116(6)]

Table 5.3 shows the experimental alloy scattering intensities and Fig. 5.10 compares the experimental I_{LM} with the theoretical Laue monotonic intensities from Eq. 2.4 based on random alloying. As one can see, theory and experiment agree well until the x is greater than 0.050.

Table 5.3 Experimental alloy scattering intensities in electron units. (a) as-rolled samples, (b) annealed samples (400°C × 5 h).

Sample	#2a	#3a	#4a	#5a
I_{LM}(e/a)	7.7(3)	14.5(6)	18.5(8)	22.3(9)

(a)

Sample	#2ah	#3ah	#4ah	#5ah
I_{LM}(e/a)	7.9(4)	14.8(6)	18.7(8)	23.6(9)

(b)

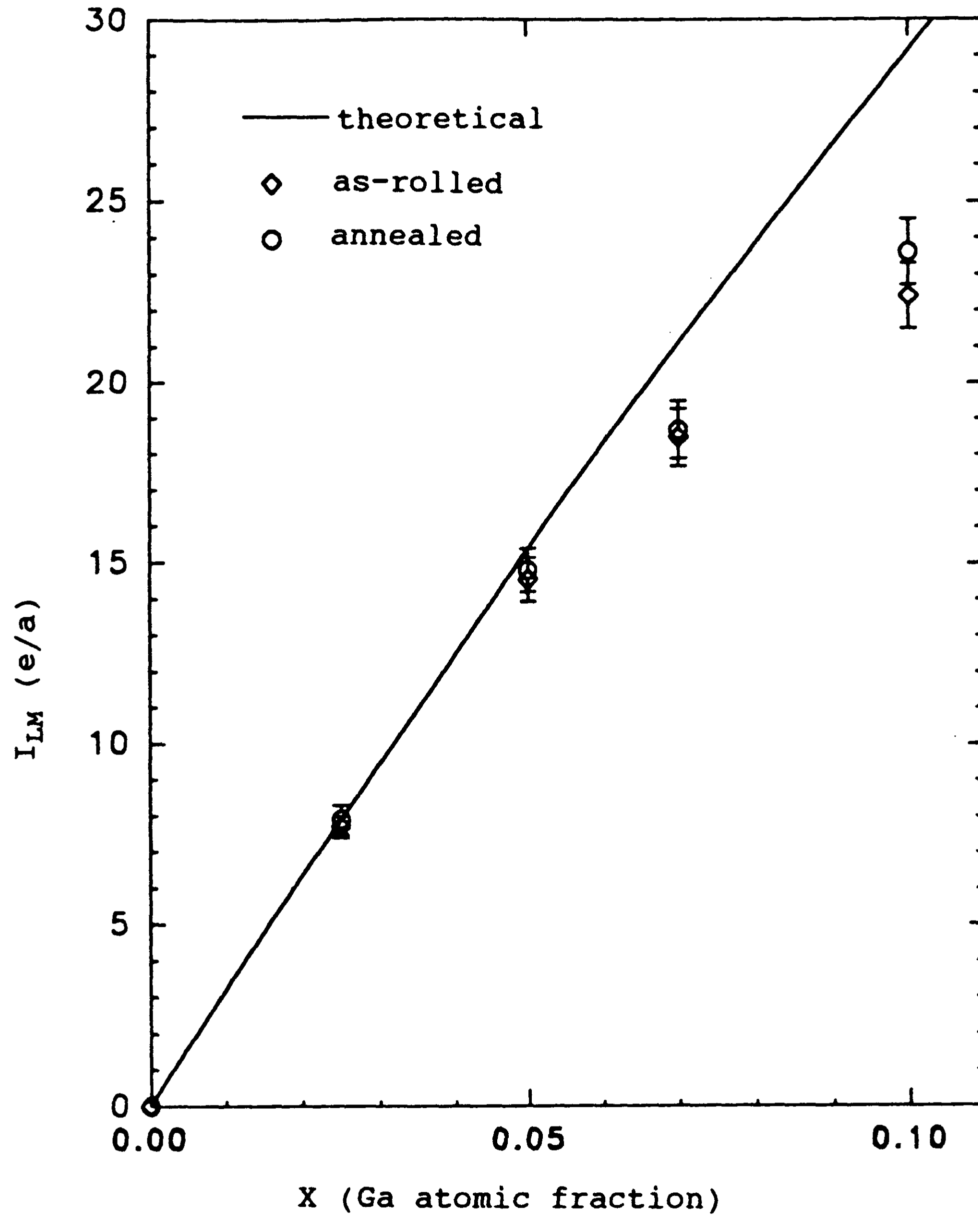

Figure 5.10 Theoretical and experimental Laue monotonic intensities for $Al_{1-x}Ga_x$ alloys.

The discrepancies for x=0.070 and x=0.100 are attributed to Ga precipitation in these samples. In Fig. 5.10, the difference between the experimental data points and the theoretical curve can provide the quantitative amount of Ga precipitation. Table 5.4a gives the numerical values of the breakdown of Ga in solid solution in the random alloy (x_s) and as Ga precipitates (x_p).

In Table 5.4b, x_p using V_f based on Q is much smaller compared to that calculated by using I_{LM}, because of missing Q due to very large Ga precipitates which can not be detected.

Table 5.4 Amount of Ga in solid solution (x_s) and as Ga precipitates (x_p) based on (a) difference in experimental and theoretical I_{LM} and (b) experimental integrated SAXS intensities (Q, V_f from table 5.2).

Sample	#2a [#2ah]	#3a [#3ah]	#4a [#4ah]	#5a [#5ah]
x_s	0.0244(10) [0.0250(13)]	0.0470(19) [0.0480(19)]	0.0608(28) [0.0615(28)]	0.0744(32) [0.0791(32)]
x_p	0.0006(10) [0.0000]	0.0030(19) [0.0020(19)]	0.0092(28) [0.0085(28)]	0.0256(32) [0.0209(32)]
x_s+x_p	0.0250	0.0500	0.0700	0.1000

(a)

Sample	#2a [#2ah]	#3a [#3ah]	#4a [#4ah]	#5a [#5ah]
x_s	0.0250 [0.0250]	0.0494(2) [0.0495(2)]	0.0688(3) [0.0694(2)]	0.0968(3) [0.0990(2)]
x_p	0.0000 [0.0000]	0.0006(2) [0.0005(2)]	0.0012(3) [0.0006(2)]	0.0032(3) [0.0010(2)]
x_s+x_p	0.0250	0.0500	0.0700	0.1000

(b)

Table 5.4a shows that there is significant difference in the amount of Ga precipitation (calculated by using I_{LM}) between the as-rolled series and the annealed series. This shows the annealing effect (more lattice diffusion of Ga into solid solution) of alloys. Combining the two results shows that the annealing promotes diffusion of Ga into the matrix, and also helps the growth of the Ga precipitates, such that Q is reduced for the experimental q range. In table 5.4b, the x_s values are larger, but these values are not acceptable, because large Ga precipitates were not detected by SAXS (the Q values used to calculate x_p.values were underestimated). Therefore, the x_s and x_p values in table 5.4a are considered to be more accurate.

In order to examine the possible shape of the Ga precipitates detected by SAXS, the integral invariant ratio

Q_0/Q_{45} from 0 and 45 degree tilting was measured. This method qualitatively measures the presence of oriented, non-spherical features. Table 5.5 shows the integral invariant ratio Q_0/Q_{45} of one set of alloys.

Table 5.5 The integral invariant ratio Q_0/Q_{45} with increase of x.

Sample	#1ah	#2ah	#3ah	#4ah	#5ah
Q_0/Q_{45}	0.9(2)	1.0(3)	1.2(4)	1.3(2)	0.9(2)

When this ratio is less than unity, the scattering objects are plate-like and oriented parallel to the sample surface, but a ratio greater than unity suggests the objects are rod-like and perpendicular to the sample surface. Sphere or randomly-oriented non-spheres yield a ratio of unity. As one can see in the Table 5.5, the ratio Q_0/Q_{45} of the annealed series is close to unity. This suggests that the Ga precipitates are randomly oriented or spherical in shape.

5.3.3 Correction of Lattice Parameter Data by SAXS Results

In view of the significant amount of Ga precipitation in the x=0.070 and 0.100 alloys, corrections need to be made

to the XRD data presented earlier in Fig. 5.7. Using the numerical amount of Ga in solid solution (x_s) in table 5.4a, lattice parameters are replotted in Fig. 5.11. The quality of the fits were substantially improved as indicated by the better linearity compared to Fig. 5.7. For the improvement of a_3 fit in Fig. 5.11, the x_s values of as-rolled samples were used because there is negligible lattice diffusion of Ga in solid solution at room temperature.

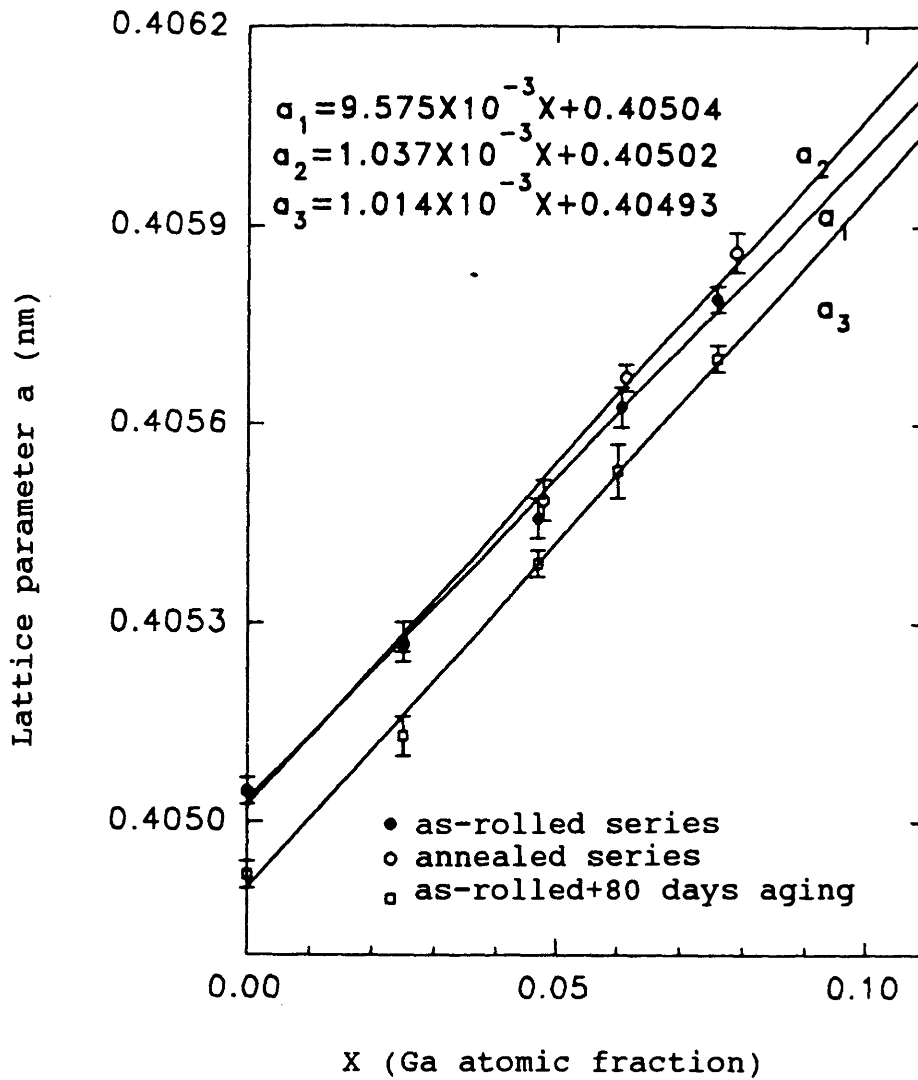

Figure 5.11 Lattice parameter versus Ga atomic fraction x after correction of x by SAXS results. a_1 is the fit of as-rolled series. a_2 is the fit of annealed series. a_3 is the fit of aged series.

Chapter 6

Summary and Conclusion

A set of $Al_{1-x}Ga_x$ alloys with $0 \leq x \leq 0.10$ has been prepared and investigated by small-angle x-ray scattering and x-ray diffraction. The comparison between experimental alloy scattering, which was detected by SAXS, and theoretical Laue monotonic scattering provided information on the randomness of the $Al_{1-x}Ga_x$ alloys and the accuracy of conversion of the x-ray intensity to absolute units. Tests were made of the slit smearing effect on the SAXS signal and of the infinite slit approximation. X-ray diffraction combined with the SAXS results led to a precise determination of the effect of x on the lattice parameter of the fcc solid solution phase. Specific experimental results can be summarized as follows.

i) The maximum solubility of Ga in Al obtained from analysis of alloy scattering intensity by SAXS is 7.90(7) at.%. This value was reached by annealing a sample containing 10 at.% Ga at 400°C for 5 hours. According to several published papers [23, 27, 43], the maximum solubility (interpolated from the phase diagram) of Ga in Al at room temperature by means of thermal analysis has quite a large uncertainty

because of uncertainty in the solidus temperature. The estimated maximum solubility range from the published papers is from about 8.7 at.% to 10 at.%. Further refinement of the heat treatment procedure used here could lead to larger amount of Ga in random solution.

ii) The theoretical and experimental alloy scattering intensities agree very well for Ga concentrations of 2.5 at.% and 5 at.%. But for nominal concentrations of 7 at.% and 10 at.%, clear discrepancies occur. This is due to Ga precipitates in alloys as detected by SAXS. The tilting study suggests the precipitates are randomly oriented or spherical in shape. The annealing ($400^{\circ}C \times 5$ hr) after cold-work induced a size increase of the precipitates such that the largest particles exceeded the SAXS detection scale ($R \geq 15$ nm). Also, the annealing caused some additional lattice diffusion of Ga into solid solution for the 10 at.% Ga sample.

Table 5.4a provides the numerical values of the amount of Ga in random solid solution, x_s, for all samples investigated.

iii) The fcc lattice parameters of the $Al_{1-x}Ga_x$ alloys increase linearly with x. The linear fits of lattice

parameter versus x were corrected with the SAXS-determined amount of Ga in solid solution (x_s). This led to the fits shown in Figure 5.11. It is interesting that both the as-rolled and the annealed series of data lie above the room-temperature-aged data by approximately a constant shift of 0.0001 nm. Stress relief of the as-rolled series is a reasonable explanation but it seems that the 400°C annealing should have a similar stress-recovery effect. To our knowledge, this is the first determination of the lattice parameter for a systematic series of $Al_{1-x}Ga_x$ alloys.

iv) The slit smearing correction was tested with our standard polyethylene sample. The result clearly shows how the SAXS signal is distorted in the small q region ($0 \leq q \leq 2$ nm^{-1}), and that it approaches the intensity of pinhole collimation in the range $q \geq 2.5$ nm^{-1}. From the measure slit length weighting function, P(t), conversion of the pinhole SAXS data to line collimation data yielded excellent agreement between the two sets of experimental data.

From the results of the slit smearing study, it is clear that the alloy scattering intensities are not affected by smearing because they are measured in the high q region ($4 < q < 6$ nm^{-1}).

v) The validity of the infinite slit approximation for calculation of the integral invariant, Q, in the Kratky system used here was investigated and it is concluded that this approximation is valid to within 10% when the particle size is greater than 2 nm. Smaller particles must be considered with more care in calculations of Q and the corresponding volume fraction.

Finally, the good agreement of theory and experiment for the alloy diffuse scattering intensity of the $Al_{1-x}Ga_x$ alloys studied here provides support for this method to study atomic-scale randomness in the amorphous $Si_{1-x}Ge_x$ alloys.

References

[1]. Y. Chen, *Microstructure Study of Amorphous silicon-based Semiconductors by Small Angle X-ray Scattering*, Ph.D. Thesis, Colorado School of Mines, 1994.

[2]. L. H. Schwartz and J. B. Cohen, *Diffraction from Materials* (Berlin, Spring-Verlag, 1987) p232.

[3]. A. Guinier, *X-ray Diffraction* (W. H. Freeman and Company, San Fransisco, 1963) p200.

[4]. *International Tables for X-ray Crystallography*, 1962, **Vol.3**, 247.

[5]. C. B. Walker, Phy. Rev., 1959, **103**, 558.

[6]. A. J. Freeman, Acta Cryst., 1959, **12**, 274.

[7]. A. M. Leveiut and A. Guinier, *Small Angle X-ray Scattering* (H. Brumberger (ed), Gordon and Breach, New York, 1955) p363.

[8]. B. E. Warren, Acta Cryst., 1959, **12**, 837.

[9]. E. Nold, S. Steeb, P. Lamparter, and G. Rainer-Harbach, J. Phys. (Paris) Colloq., 1980, **41**, C8.

[10]. H. Atkinson and P. B. Hirsch, Philos. Mag., 1958, **3**, 213.

[11]. E. Taglauer, Phys. Status Solidi, 1968, **29**, 259.

[12] B. K. Agarwal, *X-Ray Spectroscopy* (Springer-Verlag, New York, 1991) p283.

[13]. M. A. Singh, S. S. Ghosh and R. F. Shannon Jr., J. Appl. Cryst, 1993, **26**, 787.

[14]. Paul W. Schmidt, J. Appl. Cryst., 1988, **21**, 602.

[15]. G. Walter and P. W. Schmidt, J. Appl. Cryst., 1981, **14**, 28.

[16]. Paul W. Schmidt and Boris A. Fedorov, J. Appl. Cryst., 1978, **11**, 411.

[17]. O. Glatter, *Small Angle X-ray Scattering*, (O. Glatter and O. Kratky (eds.), Academic Press, New York, 1982) p120.

[18]. G. Porod, *Small Angle X-ray Scattering* (O. Glatter and O. Kratky (eds.), Academic Press, New York, 1982) p154.

[19]. G. Porod, *ibid.*p26.

[20]. A. Guinier and Gerard Fournet, *Small Angle Scattering of X-ray* (John Wiley & Sons, New York, 1955) P116.

[21]. J. W. H. Clare, *Note on the Determination of the Aluminum-Gallium Equilibrium Diagram*, 1959, 476.

[22]. H. Zoller, Metall, 1957, **5**, 378.

[23]. L. F. Mondolfo, *Aluminum Alloys: Structure and Properties*, Butterworths, Boston (1976).

[24]. L. A. Willey, *Metal Handbook*, 8th edition, (ASM, Material park, Ohio, 1973) p260.

[26]. J. R. Davis (ed.), *Aluminum and Aluminum Alloys* (ASM. specialty handbook, Mterial Park, Ohio, 1993) p548.

[28]. E. A. Owen, Y. H. Liu, and D. P. Morris, Phil. Mag., 1948, **39**, 831.

[27]. G. H. Bishop, Met. Trans, 1968, **242**, 1343.

[28]. H. Ichinose, Bulletin of the Faculty of Engineering, Yokohama National University, 1969, **18**, 138.

[29]. C. Elbaum, Trans. Metall. Soc. AIME, 1959, **215**, 476.

[30]. C. Roques-Carmes, M. Aucouturier and P. Lacombe, Met. Sci. J., 1973, **7**, 128.

[31]. N. L. Perterson and S. J. Rothman, Phys. Rev. B, 1970, **1**, 3264.

[32]. A. Guinier and G. Fournet, *Small Angle Scattering of X-rays* (John Wiley, New York, 1955) p116.

[33].D. L. Williamson, A. H. Mahan, B. P. Nelson, and R. S. Crandall, Appl. Phys. Lett., 1989, **50**, 783.

[36]. O. Kratky, *Small Angle X-ray Scattering* (O. Glatter and O. Kratky (eds.), Academic Press, New York, 1982) p77.

[35]. P. Klug and E. Alexander, *X-ray diffraction procedures* (John Wiley & sons, New York, 1954) p591.

[36]. B. Rodmacq, Ph. Mangin, A. Chamberod, Phys. Rev. B, 1984, **30**, 6188.

[37]. W. H. Robinson and R. Smoluchowski, J. Appl. Phys., 1956, **27**, 657.

[38]. Michel Roth, J. Appl. Cryst., 1977, **10**, 172.

[39]. Sigmund and Weissmann, *Metals and Alloys* (Benzamin Post (eds.), JCPDS, Pennsylvania, 1978) p82.

[40]. G. Porod, *Small angle X-ray scattering* (O. Glatter and O. Kratky (eds.) Academic Press, New York, 1982) p26.

[41]. H. Zoller, Metall, 1957, **11**, 378.